

R05-5.300.0022

UTRC Report Number R05-5.300.0022

High Temperature Heat Exchanger Development

Daniel Sabatino
United Technologies Research Center
411 Silver Lane
East Hartford, Connecticut 06108
USA

David Scott
HS Marston Aerospace Limited
Wobaston Road, Fordhouses
Wolverhampton, WV10 6QJ
England

Prepared for
Office of Naval Research

Under Contract Number:
N00014-03-C-0444

October 2005



Research Center

REPORT DOCUMENTATION PAGE

Form Approved
OMB No. 0704-0188

Public reporting burden for this collection of information is estimated to average 1 hour per response, including the time for reviewing instructions, searching existing data sources, gathering and maintaining the data needed, and completing and reviewing this collection of information. Send comments regarding this burden estimate or any other aspect of this collection of information, including suggestions for reducing this burden to Department of Defense, Washington Headquarters Services, Directorate for Information Operations and Reports (0704-0188), 1215 Jefferson Davis Highway, Suite 1204, Arlington, VA 22202-4302. Respondents should be aware that notwithstanding any other provision of law, no person shall be subject to any penalty for failing to comply with a collection of information if it does not display a currently valid OMB control number. **PLEASE DO NOT RETURN YOUR FORM TO THE ABOVE ADDRESS.**

1. REPORT DATE (DD-MM-YYYY) 17-11-2005		2. REPORT TYPE Final		3. DATES COVERED (From - To) 9-25-2003 to 14-12-2003	
4. TITLE AND SUBTITLE High Temperature Heat Exchanger Development				5a. CONTRACT NUMBER N00014-03-C-0444	
				5b. GRANT NUMBER	
				5c. PROGRAM ELEMENT NUMBER	
6. AUTHOR(S) Sabatino, Daniel R; Author Scott, David R; Author				5d. PROJECT NUMBER	
				5e. TASK NUMBER	
				5f. WORK UNIT NUMBER	
7. PERFORMING ORGANIZATION NAME(S) AND ADDRESS(ES) United Technologies Research Center 411 Silver Lane East Hartford, CT 06108				8. PERFORMING ORGANIZATION REPORT NUMBER R05-5.300.0022	
HS Marston Aerospace Limited Wobaston Road, Fordhouses Wolverhampton, WV10 6QJ England					
9. SPONSORING / MONITORING AGENCY NAME(S) AND ADDRESS(ES) Office of Naval Research One Liberty Center 875 North Randolph Street, Arlington, VA 22203-1995				10. SPONSOR/MONITOR'S ACRONYM(S) ONR	
				11. SPONSOR/MONITOR'S REPORT NUMBER(S)	
12. DISTRIBUTION / AVAILABILITY STATEMENT A Approved for public release					
13. SUPPLEMENTARY NOTES					
14. ABSTRACT Gas turbine engines have long used fuel on its way to the combustor as a coolant for engine components. Advanced aircraft and engine technologies are demanding more cooling capacity than conventional fuel delivery systems can offer. To meet these new cooling requirements, technologies are being pursued to allow fuel to reach significantly higher temperatures without the traditional limitations associated with coking. A compact fuel/air heat exchanger is a critical component in these new high-temperature fuel systems. Both tubular metal foam and hollow-truss cellular metal heat exchangers were examined for performance, size, and weight benefits as compared to conventional shell-tube technology. The application of interest was based on advanced thermal management system concepts targeted for the 5 percent JSF growth engine. The tubular metal foam heat exchanger behavior was characterized with scaled laboratory and full-scale rig experiments. The data were used to calibrate an analytical model based on data in the open literature. The results indicate that sintered metal foam can provide as much as twice the heat transfer as a plain bank of staggered tubes. However, the corresponding 4X increase in pressure drop almost neutralizes the heat transfer benefit. Furthermore, it was determined that metal foam manufacturing constraints combined with the small high pressure fuel tubes would result in a design which has no size/weight or performance benefit compared to a traditional shell-tube unit. However a 40 percent reduction in the number of tubes may provide improved reliability. Finally, a preliminary investigation of a hollow-tube cellular metal heat exchanger found that when elliptical non-flowing rods are used to augment the tube-bank they can increase the heat transfer by as much as 1.5X over a plain staggered tube-bank without a significant increase in pressure drop. It is projected that 10 percent weight and 30 percent size reductions can be achieved with hollow-truss cellular metal as compared to shell-tube heat exchanger. However, this estimate is based on extrapolations from test data. Furthermore, realization of hollow-tub cellular metal may require a costly manufacturing process.					
15. SUBJECT TERMS High Temperature Heat Exchanger; Heat Exchanger; Metal Foam; Aerospace Heat Exchanger; Metal Foam Heat Exchanger; Cellular Metal; Hollow Truss Cellular Metal; Cellular Metal Heat Exchanger					
16. SECURITY CLASSIFICATION OF:			17. LIMITATION OF ABSTRACT Unclassified Unlimited	18. NUMBER OF PAGES 54	19a. NAME OF RESPONSIBLE PERSON Daniel Sabatino
a. REPORT UNCLASSIFIED	b. ABSTRACT UNCLASSIFIED	c. THIS PAGE UNCLASSIFIED			19b. TELEPHONE NUMBER (include area code) 860-610-7273

Abstract

Gas turbine engines have long used fuel on its way to the combustor as a coolant for engine components. Advanced aircraft and engine technologies are demanding more cooling capacity than conventional fuel delivery systems can offer. To meet these new cooling requirements, technologies are being pursued to allow fuel to reach significantly higher temperatures without the traditional limitations associated with coking. A compact fuel/air heat exchanger is a critical component in these new high-temperature fuel systems. Both tubular metal foam and hollow-truss cellular metal heat exchangers were examined for performance, size, and weight benefits as compared to conventional shell-tube technology. The application of interest was based on advanced thermal management system concepts targeted for the 5 percent JSF growth engine. The tubular metal foam heat exchanger behavior was characterized with scaled laboratory and full-scale rig experiments. The data were used to calibrate an analytical model based on data in the open literature. The results indicate that sintered metal foam can provide as much as twice the heat transfer as a plain bank of staggered tubes. However, the corresponding 4X increase in pressure drop almost neutralizes the heat transfer benefit. Furthermore, it was determined that metal foam manufacturing constraints combined with the small high pressure fuel tubes would result in a design which has no size/weight or performance benefit compared to a traditional shell-tube unit. However a 40 percent reduction in the number of tubes may provide improved reliability. Finally, a preliminary investigation of a hollow-tube cellular metal heat exchanger found that when elliptical non-flowing rods are used to augment the tube-bank they can increase the heat transfer by as much as 1.5X over a plain staggered tube-bank without a significant increase in pressure drop. It is projected that 10 percent weight and 30 percent size reductions can be achieved with hollow-truss cellular metal as compared to shell-tube heat exchanger. However, this estimate is based on extrapolations from test data. Furthermore, realization of hollow-tub cellular metal may require a costly manufacturing process.

Foreword

This report summarizes work performed under the Office of Naval Research Contract N00014-03-C-0444. Dr. Steven Fishman of the Office of Naval Research , Arlington VA administered the contract.

The program manager at UTRC for this contract was Dr. Daniel Sabatino. The authors gratefully acknowledge Don Floyd (Porvair Fuel Cells), who provided a great deal of assistance and guidance in understanding metal foam manufacture and performance. We would also like to thank Fabio Bertolotti (UTRC) for his CFD expertise and Larry Pryor (UTRC) for his attention to detail and assistance in executing the single tube-row metal foam experiments.

Table of Contents

Abstract	ii
List of Tables.....	viii
Nomenclature	x
1.0 Introduction	1
2.0 Experimental Methods	3
2.1 Single Tube Row Experiments	3
2.2 Tube-Bank Experiments	6
3.0 Tubular Metal Foam Results	8
3.1 Analytical Model.....	8
3.2 Single-Row Experimental Results	11
3.3 Comparison to CFD model	20
3.4 Tube-Bank Experimental Results	22
3.5 Design Optimization	26
4.0 Cellular Metal Results	30
4.1 Cellular Metal Tube-Bank Experimental and CFD Results.....	30
4.2 Cellular Metal Design Optimization	38
5.0 Summary and Conclusions	41
6.0 References	43
7.0 Appendix	44
7.1 Single Tube-Row Metal Foam Experimental Data (UTRC)	44
7.2 Single Tube-Row Metal Foam Experimental Data (HS Marston).....	51
7.3 Tube-Bank Data	55
7.3.1 Pressure Drop Performance	55
7.3.2 Heat Transfer Performance.....	57
7.4 CFD Results	60
7.5 Full-Size Demonstration Unit	62

List of Figures

Figure 1.1	Example of a tubular metal foam heat exchanger.....	2
Figure 1.2	Example of a cellular metal truss. (Queheillat, 2003).....	3
Figure 2.1	Typical test sample employed in UTRC test facility. All dimensions in inches.....	4
Figure 2.2	Experimental arrangement for two dimensional sample testing at UTRC.	5
Figure 2.3	Cross-section of air side flow distribution for UTRC single tube row experiments	5
Figure 2.4	HS Marston test section for measuring pressure drop and performance of single tube row metal foam samples.....	6
Figure 2.5	Typical tube-bank sample with flow direction indicated.....	7
Figure 2.5	Tube-bank experiment setup.....	7
Figure 2.6	Side view of reference inline (aligned) and staggered tube arrangements.....	8
Figure 3.1	Haack et al. (2001) data showing the relationship between Nusselt number and Reynolds number for various foams	9
Figure 3.2	Scaled photographs of the metal foam samples employed in the single tube row experiments. All samples brazed except were noted.	12
Figure 3.5	Pressure drop for 10 ppi 5% (nominal) Inconel single row sample tested at UTRC.....	14
Figure 3.11	Heat transfer for 10ppi 5% (Nominal) Inconel single row sample tested at UTRC. Foam properties established by presure drop data.....	18
Figure 3.13	Heat transfer for 20ppi 10% (Nominal) Inconel single row sample tested at UTRC	19
Figure 3.17	Heat transfer for reference tube-bank samples	22
Figure 3.18	Friction factor for reference tube-bank samples	23
Figure 3.19	Reference tube-bank unit illustrating the stiffener plates required for manufacture.....	23

Figure 3.20 20ppi 5% SS metal foam tube-bank unit data with aligned and staggered tubes..... 24

Figure 3.21 Reference tube-bank unit illustrating the stiffener plates required for manufacture..... 25

Figure 3.22 Heat exchanger flow configurations considered in the optimization of the metal foam design. a) Reference baffled cross-counterflow shell-tube. b) Counterflow metal foam. c) Cross u-tube metal foam. d) Cross flow (single/multiple passes). 27

Figure 4.1 Top and side view of open cellular metal configuration..... 30

Figure 4.2 Top and side view of dense cellular metal configuration. 30

Figure 4.3 Top and side view of dense aligned cellular metal configuration..... 31

Figure 4.4 Top and side view of open staggered cellular metal configuration. 31

Figure 4.6 Comparison of cellular metal experimental and CFD predicted heat transfer performance. 32

Figure 4.7 Comparison of cellular metal experimental and CFD predicted friction factor. 33

Figure 4.8 Comparison of cellular metal measured friction factor to the reference staggered tube sample. 34

Figure 4.9 CFD predictions for cellular metal tube-bank samples that have been uniformly scaled such that the the aligned tube-bank predictions closely match the analytical model. 35

Figure 4.10 CFD predictions of heat transfer performance for different cellular metal configurations..... 36

Figure 4.11 Scaled CFD predictions of pressure drop behavior in cellular metal as compared to analytical models of plain tube banks..... 36

Figure 4.12 CFD calculated heat transfer coefficient (W/m²/K) for the open cellular metal configuration. 37

Figure 4.13 CFD calculated heat transfer coefficient (W/m²/K) for the open cellular metal with elliptical rods (4:1 aspect ratio)..... 38

Figure 7.1 General arrangement of metal foam engine demonstration unit..... 62

Figure 7.2 Cross section of metal foam engine demonstration unit showing 3 air passes with both aligned and staggered tube arrangements 63

R05-5.300.0022

List of Tables

Table 3.1 Full size heat exchanger application performance requirements	26
Table 3.2 Optimal metal foam heat exchanger configurations vs. baseline shell-tube. All configurations have equivalent heat transfer performance.	29
Table 4.1 Open cellular metal configuraiton with elliptical rods compared to conventional shell-tube heat exchanger for Table 3.1 conditions. All configurations have equivalent heat transfer performance.	39
Table 7.1 Metal Foam UTRC Test 9 Data	44
Table 7.2 Metal Foam UTRC Test 10 Data	44
Table 7.3 Metal Foam UTRC Test 11 Data	45
Table 7.4 Metal Foam UTRC Test 12 Data	45
Table 7.5 Metal Foam UTRC Test 13 Data	46
Table 7.6 Metal Foam UTRC Test 14 Data	47
Table 7.7 Metal Foam UTRC Test 24 Data	47
Table 7.8 Metal Foam UTRC Test 25 Data	48
Table 7.9 Metal Foam UTRC Test 26A Data	49
Table 7.10 Metal Foam UTRC Test 27A Data	49
Table 7.11 Metal Foam UTRC Test 29 Data	50
Table 7.12 Metal Foam UTRC Test 30A Data	50
Table 7.13 Brazed 20ppi 10% stainless steel with 0.4pps air flow	51
Table 7.14 Brazed 20ppi 10% stainless steel with 0.6pps air flow	52
Table 7.15 Brazed 20ppi 10% stainless steel with 0.8pps air flow	52
Table 7.16 Brazed 20ppi 10% stainless steel with 1.0 pps air flow	53
Table 7.17 Brazed 20ppi 10% stainless steel pressure drop.....	54
Table 7.18 No-Braze 20ppi 10% stainless steelpressure drop	54
Table 7.19 10ppi 5% stainless steel pressure drop.....	55

Table 7.20 Dense and open cellular metal pressure drop data 55

Table 7.21 Plain aligned and staggered tube bank pressure drop data..... 56

Table 7.22 Aligned and staggered metal foam pressure drop data 57

Table 7.23 Dense cellular metal heat transfer performance data 57

Table 7.24 Open cellular metal heat transfer performance data..... 58

Table 7.25 Aligned metal foam heat transfer performance data 58

Table 7.26 Staggered metal foam heat transfer performance data 59

Table 7.27 Plain aligned tube-bank heat transfer performance data 59

Table 7.28 Plain staggered tube-bank heat transfer performance data..... 60

Table 7.29 Dense cellular metal CFD prediction for a single periodic element 60

Table 7.30 Dense aligned cellular metal CFD prediction for a single periodic element 61

Table 7.31 Open cellular metal CFD prediction for a single periodic element 61

Table 7.32 Open elliptical cellular metal CFD prediction for a single periodic element 61

Table 7.33 Open staggered cellular metal CFD prediction for a single periodic element 61

Table 7.34 Aligned tube-bank reference CFD prediction for a single periodic element 61

Nomenclature

C	inertial coefficient
Dh	hydraulic diameter
f	Fanning friction factor
j	Colburn factor
k	thermal conductivity
k_{eff}	effective thermal conductivity of foam and fluid
k_{air}	thermal conductivity of air
k_{foam}	thermal conductivity of foam
K	permeability
L	length in flow direction
μ	dynamic viscosity
Nu_K	Nusselt number based on permeability
P	pressure
Pr	Prandlt number
Re_K	Reynolds number based on permeability
ppi	pores per inch
ρ	density
ϕ	porosity
V	Darcy velocity

1.0 Introduction

Future aircraft systems will demand more cooling capacity from the engine fuel system and are projected to operate at high Mach numbers where ram air sinks will not meet the cooling requirements. Furthermore, rejecting heat to the fuel provides benefits to the engine thermodynamic cycle including reduced fuel consumption and a potential reduction in emissions.

The high cooling requirements of advanced engine thermal management systems will require the use of a fuel that can be heated well above the conventional maximum allowable temperatures. One concept is cooled cooling air (CCA), which uses fuel to cool high-pressure compressor (HPC) bleed air for subsequent use as turbine cooling air. This technology is being considered for both commercial and military applications. Long range strike (LRS) studies performed by Pratt and Whitney, UTRC and AFRL have projected that the fuel-cooled thermal management system could reduce the high-pressure turbine rotor cooling temperature by 350 F, increase takeoff thrust by 7.5%, reduce cruise TSFC by 4.5%, and provide a significant reduction in aircraft takeoff gross weight.

Nearer term concepts include growth variants of the F-135 engine utilized by the JSF. In this case, fuel could be used to cool environmental control system (ECS) bleed air that would eliminate the current fan-duct heat exchangers. A recent study performed at UTRC suggests that a conventional shell-tube design for the application would weigh approximately 100 lbm. This will clearly present a weight and packaging challenge to achieve the full system level benefit.

Both metal foam and hollow-truss cellular metal were examined as a means to augment the heat transfer of a conventional shell-tube design. A shell-tube design is the conventional technology baseline for these applications due to the high temperature and pressure requirements associated with the fuel system. The metal foam is attractive because it is light (typically 10-20% the density of solid metal) but still has a large surface area and acts to prevent the formation of boundary layers as a gas flows through it (Hunt and Tien, 1988; Calmidi and Mahajan, 1999). Sabatino et al. (2004) reported on the manufacturability of a shell and tube heat exchanger augmented with sintered metal foam.

The current work examines the optimal configuration and maximum potential benefits. An example metal foam heat exchanger is shown in Figure 1.1.



Figure 1.1 Example of a tubular metal foam heat exchanger

The hollow-truss cellular metal design is similar to that shown in Figure 1.2. It is simply a matrix of hollow rods, but in the present work, rods in one direction are used to provide a means for the fuel to flow, while the orthogonal rods provide strength and heat transfer augmentation. Cellular metal is potentially more attractive than metal foam because the geometry is more directly controlled in the manufacturing process, as compared to the random nature of the metal foam. Additionally, Wadley et al. (2003) found that the truss cellular metal can be as much as 10X stronger than metal foam. The present work seeks to understand if there is a fundamental benefit of a cellular metal configuration as compared with a conventional shell-tube design.

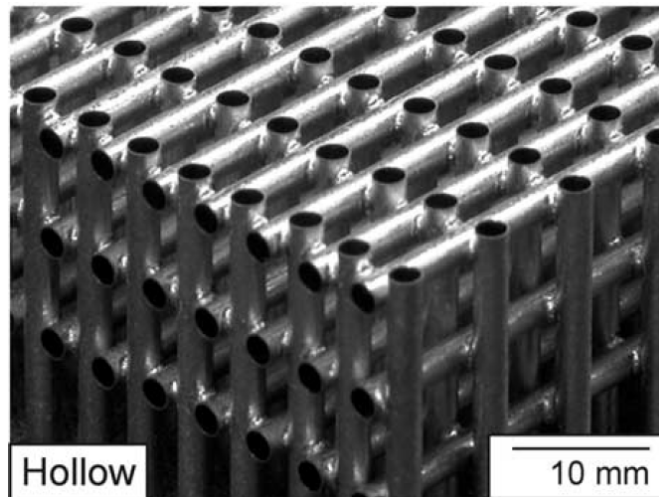


Figure 1.2 Example of a cellular metal truss. (Queheillat, 2003)

2.0 Experimental Methods

Experiments were performed at both United Technologies Research Center (UTRC) and HS Marston. Small-scale experiments were duplicated to assess reproducibility at both facilities, while larger scale tube-bank experiments were performed at HS Marston in a heat exchanger test facility that is also used to qualified production heat exchangers.

2.1 Single Tube Row Experiments

A small-scale heat exchanger facility at UTRC was employed for the initial metal foam testing. Figure 2.1 shows the details of a typical test sample, which consists of 6 tubes encased in metal foam. The samples were manufactured using two fully sintered metal foam parts, machined to receive the tubes, and sandwiching the tubes between the metal foam. The entire assembly was then brazed to permanently bond the foam and tubes. To eliminate thermal stresses, the tubes and foam were fabricated of the same material. As shown in Figure 2.2, steam was passed through the tubes to create a constant tube temperature with variable air mass flow through the metal foam. This allows the change in the air side temperature to be directly related to the performance enhancement characteristics of the foam.

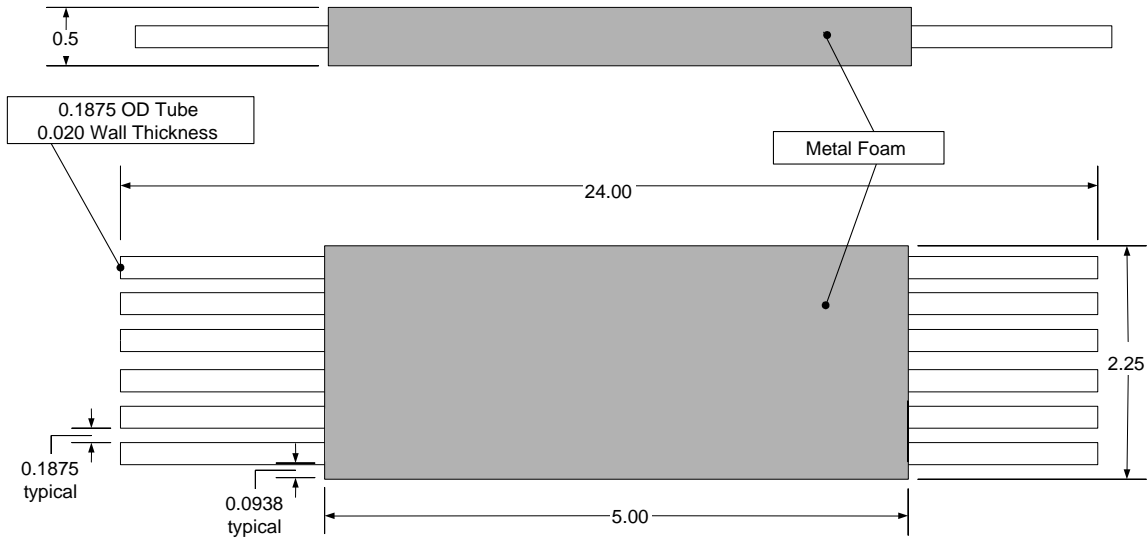


Figure 2.1 Typical test sample employed in UTRC test facility. All dimensions in inches

A continuous steam source (maximum 9 lbm/hour) supplied approximately 300 F steam to the tubes and a 400 psi air system provided dried air to the metal foam side at rates up to 0.1 lbm/s. Figure 2.3 shows a cross section view of the air side flow path which employed a porous metal flow distributor and 2-D contraction to obtain a uniform inlet velocity profile. The mass flow was measured with a venturi flow meter and the inlet and outlet air-side temperatures were measured at three different locations along the tubes and averaged. The temperature and pressure of the steam side at both the inlet and outlet were recorded to assure that a two phase flow was present throughout the heat exchanger and thus providing a constant tube temperature.

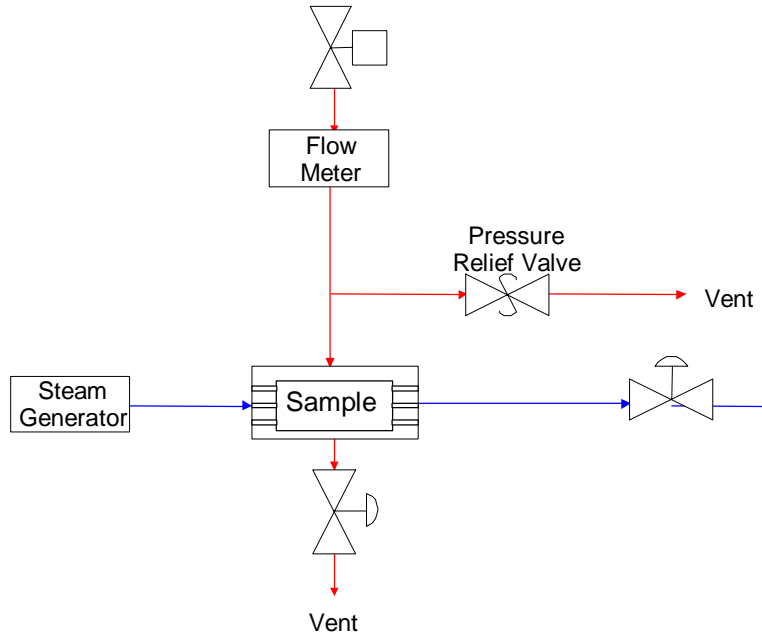


Figure 2.2 Experimental arrangement for two dimensional sample testing at UTRC.

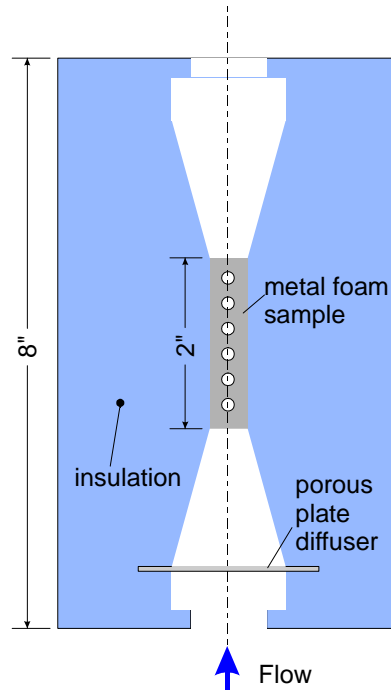


Figure 2.3 Cross-section of air side flow distribution for UTRC single tube row experiments

HS Marston repeated some of the single-tube experiments at their facility. Figure 2.4 shows the test section which held the samples. Air flow up to 0.1 lbm/s (0.045 kg/s) was delivered to the sample via draw down arrangement which provided ambient pressure air at 68FC (20C) nominal temperature to the sample air side inlet. The mass flow was measured downstream with a sharp-edged orifice. The inlet pressure and temperature were averaged from the 4 inlet and outlet taps shown in Figure 2.4. To measure the sample heat transfer performance, hot oil was passed through the tubes between 0.4 and 1.2 lbm/s (0.18 and 0.54 kg/s) with a nominal temperature of 212F (100C).

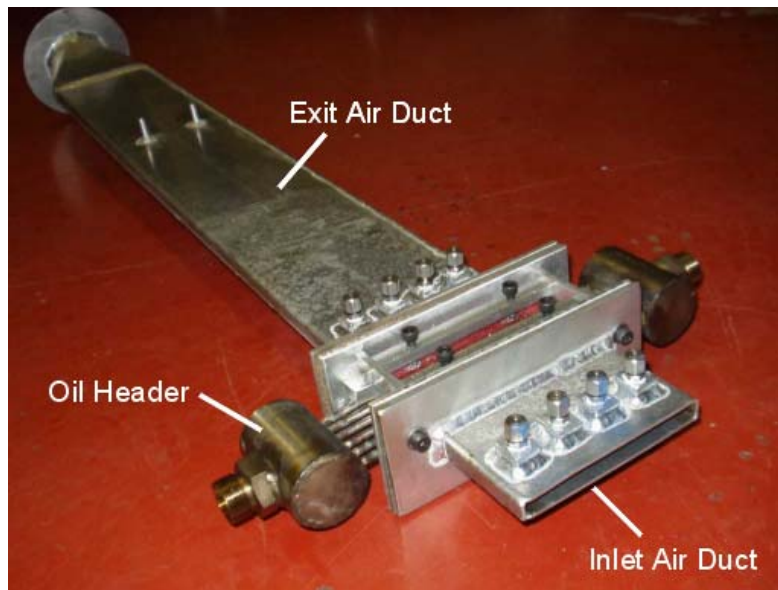


Figure 2.4 HS Marston test section for measuring pressure drop and performance of single tube row metal foam samples.

2.2 Tube-Bank Experiments

Full-scale tube-bank experiments were also performed at HS Marston in an open-loop wind tunnel that employed a hot water loop for heat exchanger performance assessment. A typical test sample is shown in Figure 2.5. All samples employed tubes with an outside diameter of 0.094 in. and a 0.007 in. wall thickness. These are conventional tube dimensions in current-technology fuel heat exchangers because the tubes must contain the high pressures (greater than 1500 psi) generated by the fuel delivery system.



Figure 2.5 Typical tube-bank sample with flow direction indicated

The inlet and outlet air-side duct was 170 x 70 mm (6.7 x 2.7 in). The heat exchanger core in each test sample was 170 x 70 x 50 mm (6.7 x 2.7 x 2.0 in). The nominal air and water supply temperature was 20C (68F) and 90C (194F) respectively. Temperature, pressure and flowrate were monitored on the inlet and outlet of both the air and water sides. A tube-bank sample installed in the facility is shown in Figure 2.6



Figure 2.5 Tube-bank experiment setup

To provide a baseline reference for both the metal foam and cellular metal results, tube-bank sample units for both an inline and staggered arrangements were fabricated. The details of the reference units are shown in Figure 2.6. For both configurations, the

minimum flow passage distance is 1 tube diameter. Note that the staggered arrangement has more tubes than the inline arrangement. The difference in absolute heat transferred because of this will be accounted for when the results are presented in nondimensional form.

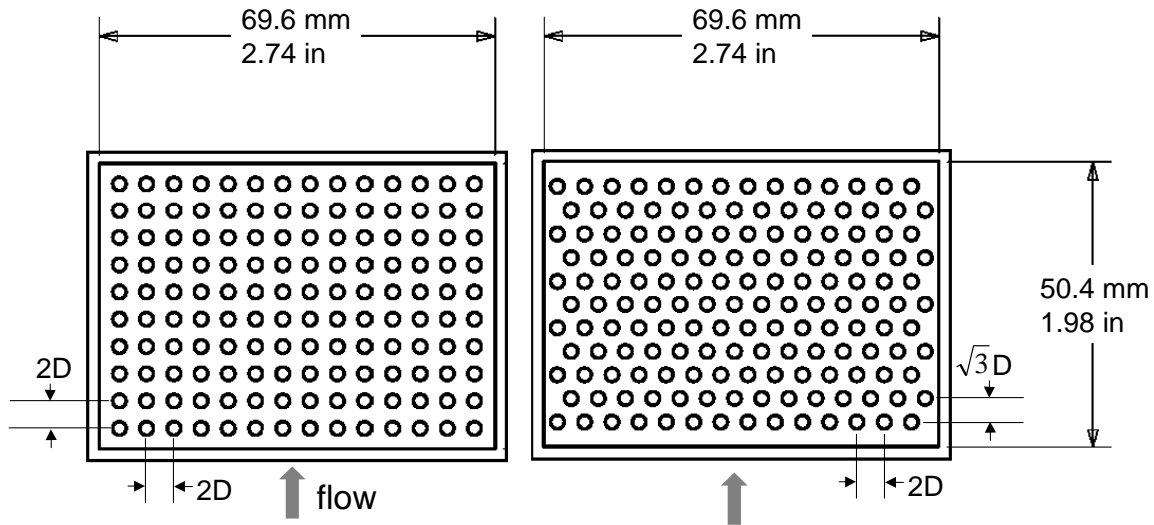


Figure 2.6 Side view of reference inline (aligned) and staggered tube arrangements.

3.0 Tubular Metal Foam Results

3.1 Analytical Model

Sabatino et al. (2004) suggested that the heat transfer of a metal foam could be predicted directly from a power law relationship between the Nusselt number and Reynolds number using the porosity, K , as the characteristic length scale. The current work seeks to refine and validate this model.

A model for sintered metal foam heat transfer behavior is based on data for several different FeCrAlY metal foams presented by Haack et al. (2001). In the current work, empirical correlations for the permeability, K , and the inertial coefficient, C , presented by Floyd (2001) were used to nondimensionalize the data. Figure 3.1 show the Nusselt number vs. the Reynolds number based on permeability for Haack's data. The figure indicates that a power law fit of the data is a meaningful correlation that can be used to predict the heat transfer behavior over the entire range of metal foams.

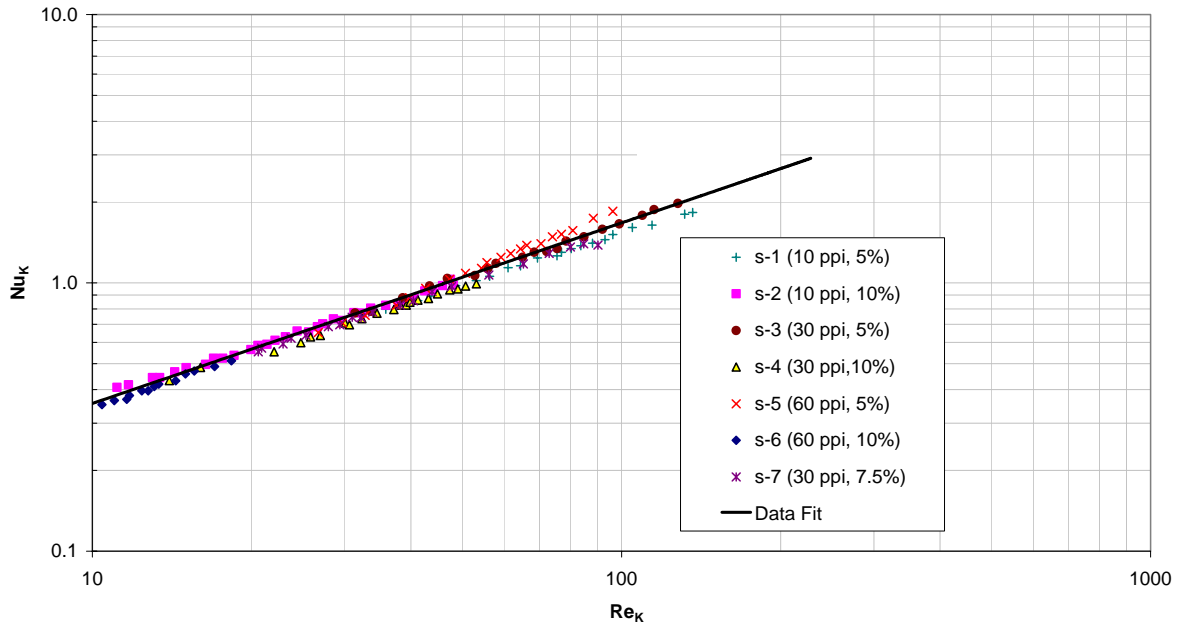


Figure 3.1 Haack et al. (2001) data showing the relationship between Nusselt number and Reynolds number for various foams

The fit shown in Figure 3.1 has the following form:

$$Nu_K = 0.0754 Re_K^{0.673} \quad (3.1)$$

where:

$$Re_K = \frac{\rho V \sqrt{K}}{\mu} \quad (3.2)$$

and the permeability is from Floyd (2001):

$$K = \left[737665(1 - \phi)^{2.06} \exp(0.0364(ppi)^{0.63}) \right]^{-1} \quad (3.3)$$

where ϕ is the *percent* porosity of the foam and *ppi* is the number of pores per inch in the foam.

Given the relationship of the Nusselt number with Reynolds number, the Colburn factor, j , can be directly calculated for the metal foam by the following:

$$j_{foam} = \frac{Nu_K}{Pr Re_K} Pr^{2/3} = \frac{0.0754}{Pr^{1/3} Re_K^{0.327}} \quad (3.4)$$

It is proposed that this relationship will be applicable to metal foam with tubes if the characteristic velocity used to calculate the Reynolds number is based on the maximum Darcy velocity, which is the bulk velocity around the tube as a result of the area contraction.

It is important to note that the heat transfer data used to develop these relationships were based on FeCrAlY samples. The experiments performed in the present study employed stainless steel and inconel foams, where inconel is the likely material of choice for the actual engine applications. Because all of these materials are relatively low conductivity metals, the impact of the different thermal conductivities is neglected. This is expected to provide reasonable conceptual predictive capability. However, if significantly different material, such as aluminum, is considered, the influence of the thermal conductivity could no longer be neglected.

It is well known Darcy's Law approximates the pressure drop through metal foam:

$$\frac{\Delta P}{L} = \frac{\mu V}{K} + C \rho V^2 \quad (3.5)$$

The inertial coefficient, C , in Equation 3.5, is given by Floyd (2001):

$$C = 1.76(1 - \phi)^{2.06} PPI^{0.63} \quad (3.6)$$

It should be noted that the inertial coefficient is sensitive to the foam density ($1 - \phi$) and when used as a coefficient for the squared velocity term in equation 3.5, makes the pressure drop very sensitive to the density. Therefore, establishing the density accurately and maintaining tight process controls would be important for any production application.

The Fanning friction factor is defined to be:

$$f = \frac{\Delta P D_h}{2L \rho V^2} \quad (3.7)$$

Note that Equation 3.7 is exactly $\frac{1}{4}$ of the Darcy friction factor, which is also commonly used (Incropera and DeWitt, 1990). Combining Equations 3.5 and 3.7, the Fanning friction factor for metal foam then becomes:

$$f_{foam} = \frac{2}{4D_h} \left(\frac{\mu}{\rho KV} + C \right) \quad (3.8)$$

For the results of the current study the hydraulic diameter, D_h , is defined as the OD of the tube (0.094 in) for simplicity. Floyd (2001) performed experiments on sintered metal foam with changing cross sectional areas and determined that the use of the average velocity was a reasonable approximation. Therefore, it is proposed that the average Darcy velocity in the foam with tubes present will best characterize the pressure drop.

3.2 Single-Row Experimental Results

Stainless steel and inconel metal foam and tube samples were tested in the facilities described in Section 2.1. The data for the samples tested are included in Appendix 7.1. The experiments were designed to better understand how the heat exchanger performance would be affected by changes in foam properties, the foam/tube bonding process as well as the material. Previously, Sabatino et al. (2004) employed metal foam that was sintered around tubes. However, based on the manufacturer's recommendation, the current work examined foam that was brazed to tubes. To understand the sensitivity of the metal foam's performance to the bonding technique, samples were tested with and without braze. Most samples were constructed of 316 stainless steel for cost and simplicity, however an inconel sample was also tested to understand the influence of the metal's thermal conductivity on the overall heat transfer performance.

Preliminary tests provided inconsistent results and prompted a close examination of the samples. Figure 3.2 shows scaled photographs of the samples tested. It can be seen that the two 10 ppi 5% density samples have a significantly different appearance. While less obvious, it is also notable that the 20ppi 10% samples are also not identical in appearance. These variations in the foam properties are an undesired result of small production runs for these laboratory tests. Although this problem would not be present in a full production run and was overcome with the tube-bank test samples discussed in

Section 3.4, it was important to determine as accurately as possible the true foam properties so the data could be properly nondimensionalized. Therefore, as is the conventional practice, the pressure drop characteristic was used to estimate the permeability and inertial coefficients, which were then used to nondimensionalize the heat transfer behavior and compare to the model presented in Section 3.1.

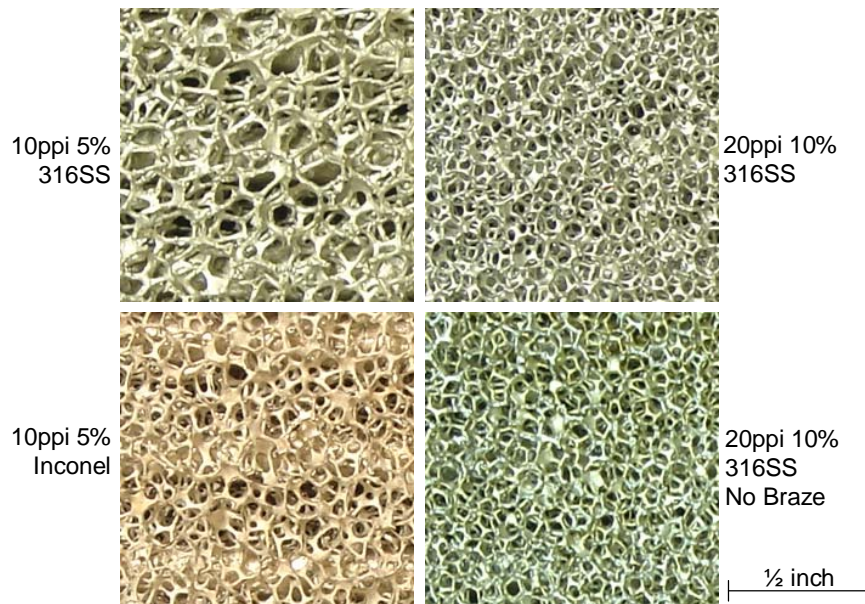


Figure 3.2 Scaled photographs of the metal foam samples employed in the single tube row experiments. All samples brazed except were noted.

Figures 3.3 and 3.4 show the pressure drop for the 20 ppi 10% (nominal) 316 stainless steel samples. One sample was brazed while the other was simply pressed together to maintain contact between the foam and tubes. Note that the data are plotted vs. the Reynolds number based on the average velocity through the tube-bank as discussed in the previous section. Because there was uncertainty about the actual foam pore size and density, Equations 3.5 and 3.5 were used to match the pressure drop and identify the foam properties implicitly. The foam properties used to generate the Darcy law fit were 18 ppi 7.5%. As expected, there is little difference in the pressure drop between the brazed and no-braze samples.

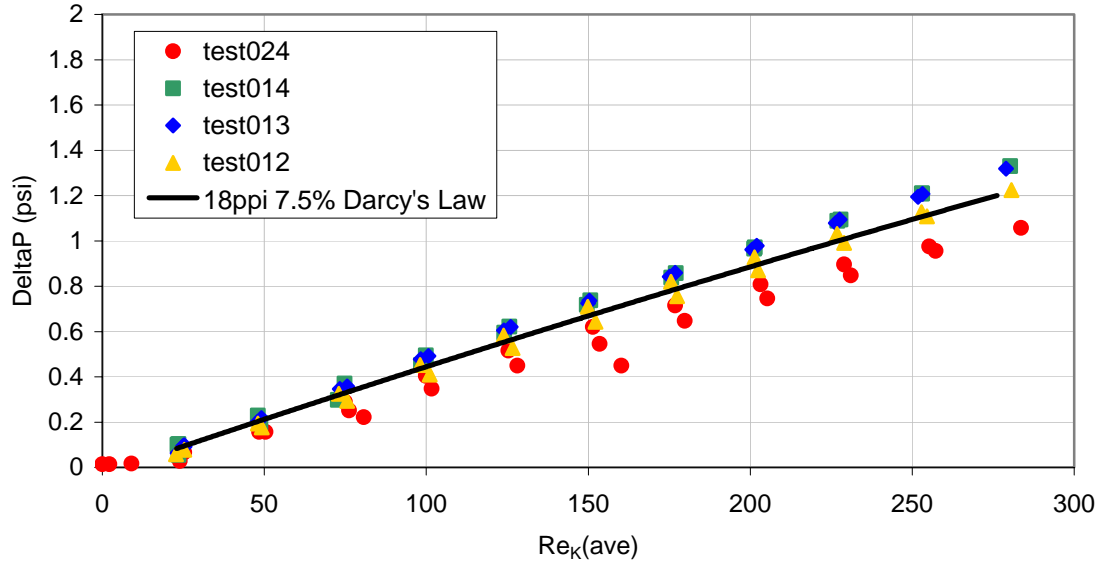


Figure 3.3 Pressure drop for 20 ppi 10% (nominal) SS brazed single row sample tested at UTRC

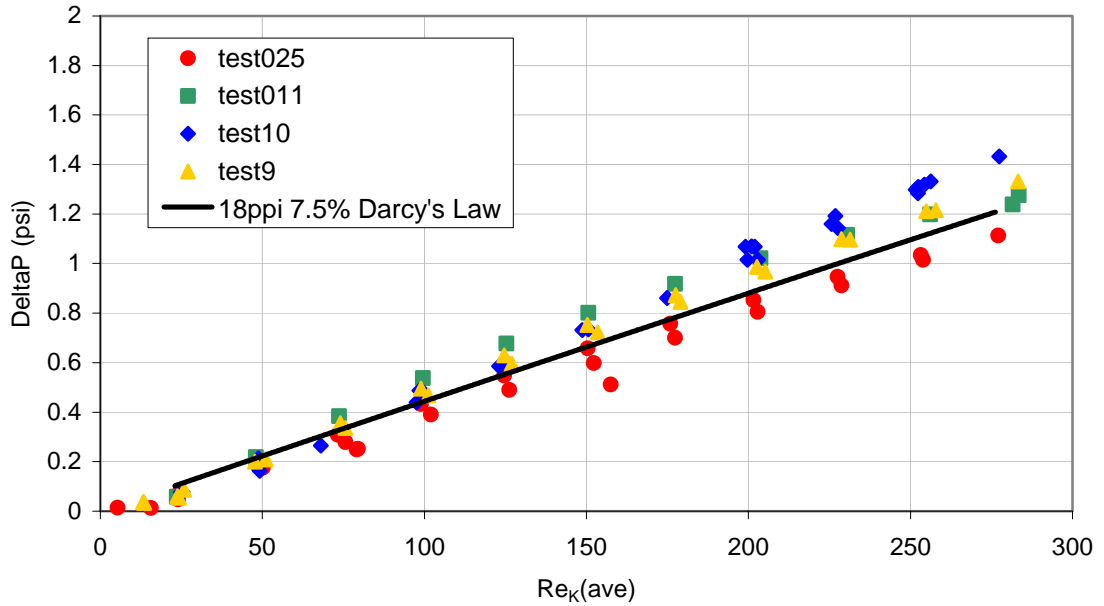


Figure 3.4 Pressure drop for 20 ppi 10% (nominal) SS no-braze single row sample tested at UTRC

The pressure drop characteristic for the Inconel sample is shown in Figure 3.5. The best fit of the data suggests a foam with 15 ppi, which is consistent with a visual inspection of Figure 3.2. Reliable pressure drop data was not recorded at UTRC for the 10 ppi 5% stainless steel sample. However, several metal foam samples were tested in the Marston single tube row test facility described in Section 2.1, including the 10 ppi 5% stainless steel sample.

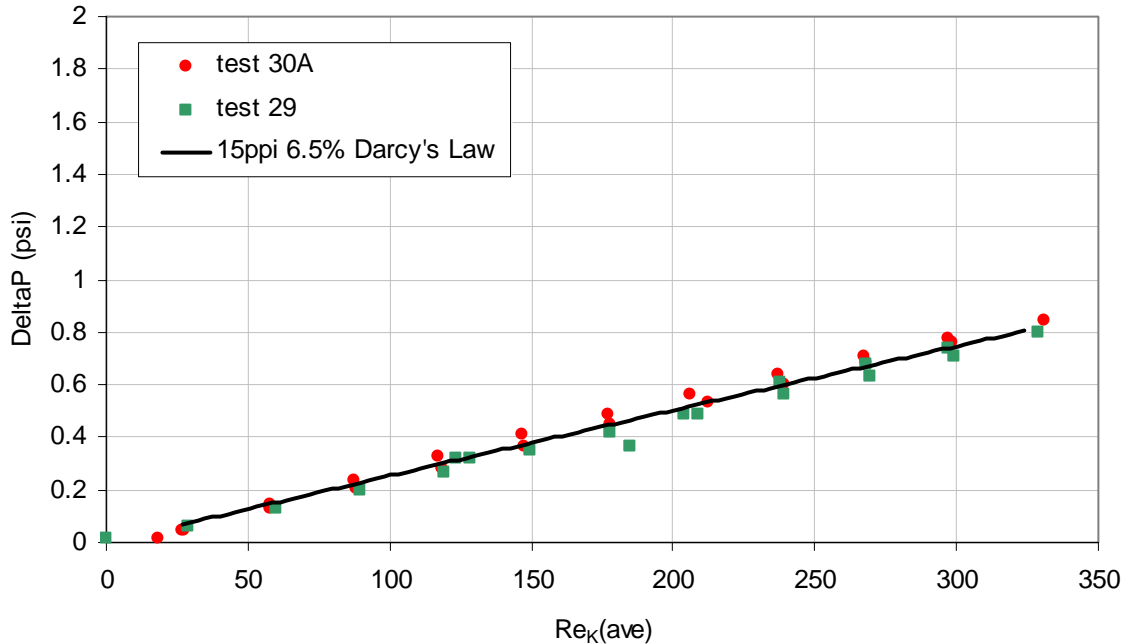


Figure 3.5 Pressure drop for 10 ppi 5% (nominal) Inconel single row sample tested at UTRC

Figures 3.6 and 3.7 show the pressure drop data for the 20 ppi and 10 ppi stainless steel single tube row samples from HS Marston. It should be noted that although the Reynolds number is in a similar range as the data presented in Figures 3.3 and 3.4, the absolute velocities associated with the data in Figure 3.6 is an order of magnitude larger because the Marston experiments employed atmospheric pressure air. This difference in the velocity magnitude is illustrated by the change in the shape of the curve and the magnitude of the pressure drop. However, the higher velocity experiments allow for a more accurate measure of the pressure drop.

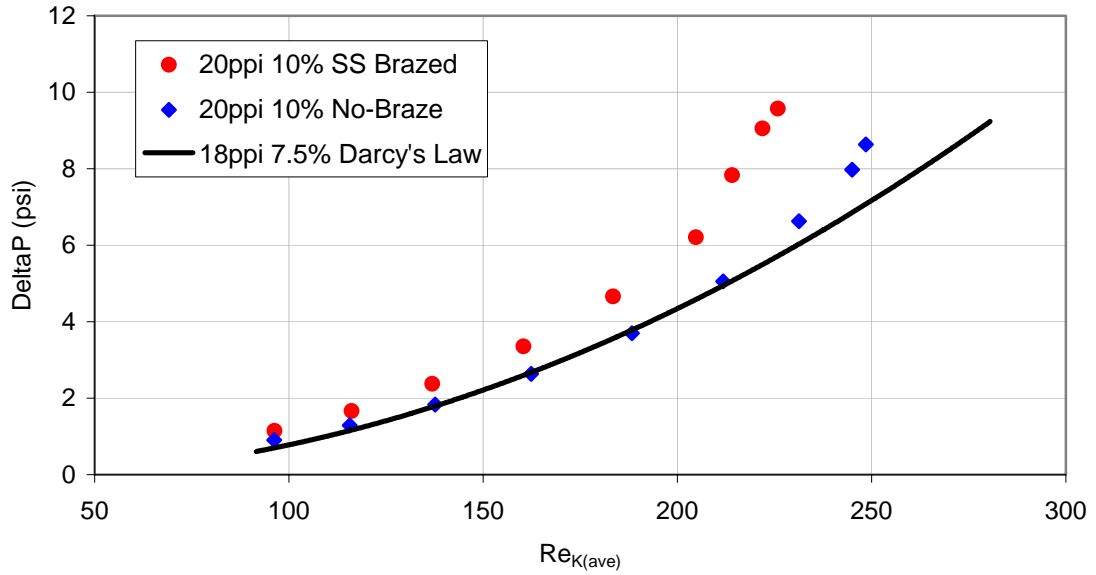


Figure 3.6 Pressure drop for 20ppi 10% (Nominal) SS – brazed and no-braze single row sample tested at HS Marston

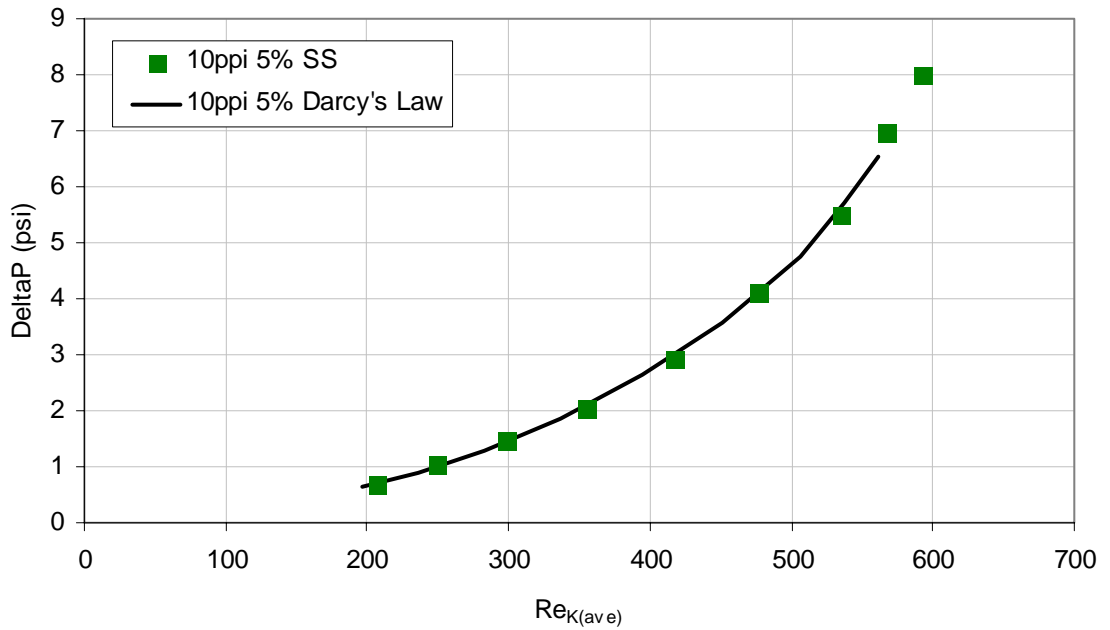


Figure 3.7 Pressure drop for 10 ppi 5% (Nominal) SS single row sample tested at HS Marston

Figure 3.6 corroborates the data recorded at UTRC shown in Figures 3.3 and 3.4. Figure 3.7 shows a pressure drop characteristic that is almost exactly as predicted by Equation 3.5 using the average velocity. All of the pressure drop data suggest that the pressure drop incurred in the foam dominates the flow behavior and that the average Darcy velocity is a reasonable way to modify the plain foam relationships to predict foam/tube behavior.

Figures 3.8 through 3.12 show the heat transfer data recorded at UTRC for the four single row samples. Equation 3.1 was used to predict the performance where the characteristic velocity is based on the maximum Darcy velocity between the tubes. The characteristic pore size and density for each sample was assumed from the pressure data described above.

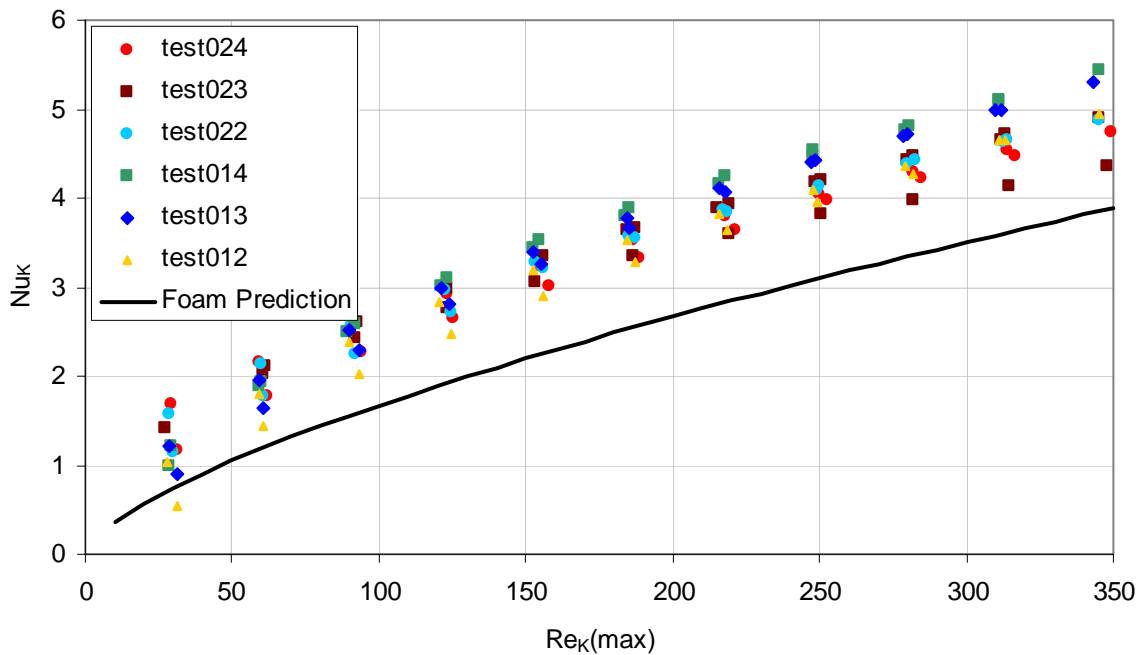


Figure 3.8 Heat transfer for 20ppi 10% (Nominal) SS brazed single row sample tested at UTRC. Foam properties established by pressure drop data.

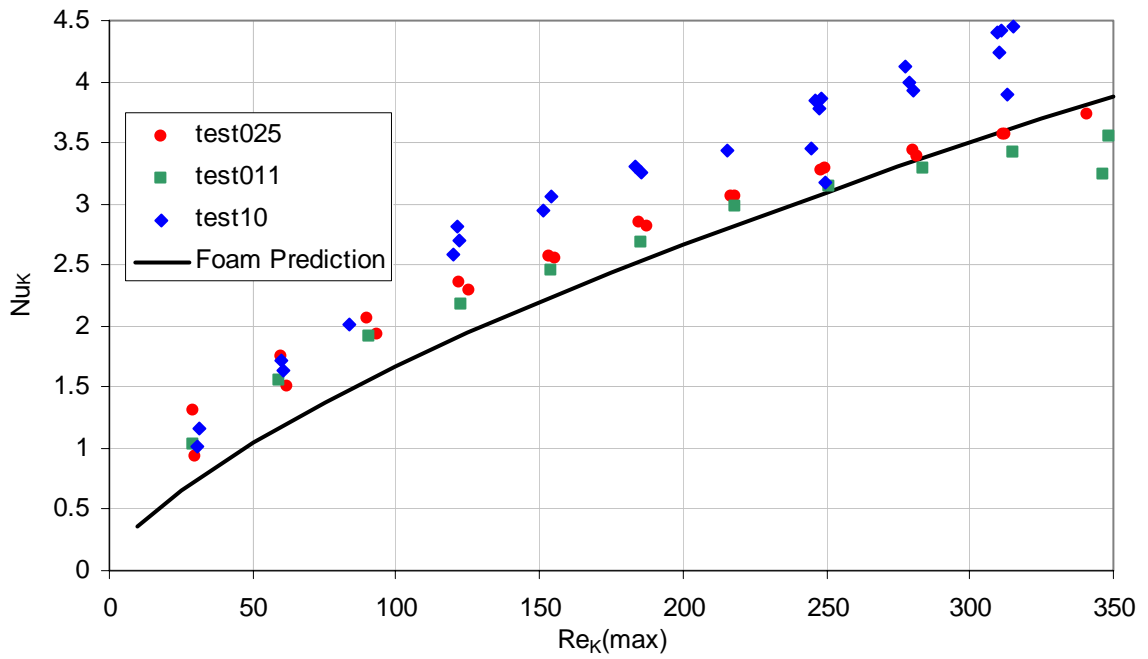


Figure 3.9 Heat transfer for 20ppi 10% (Nominal) SS no-braze single row sample tested at UTRC. Foam properties established by presure drop data.

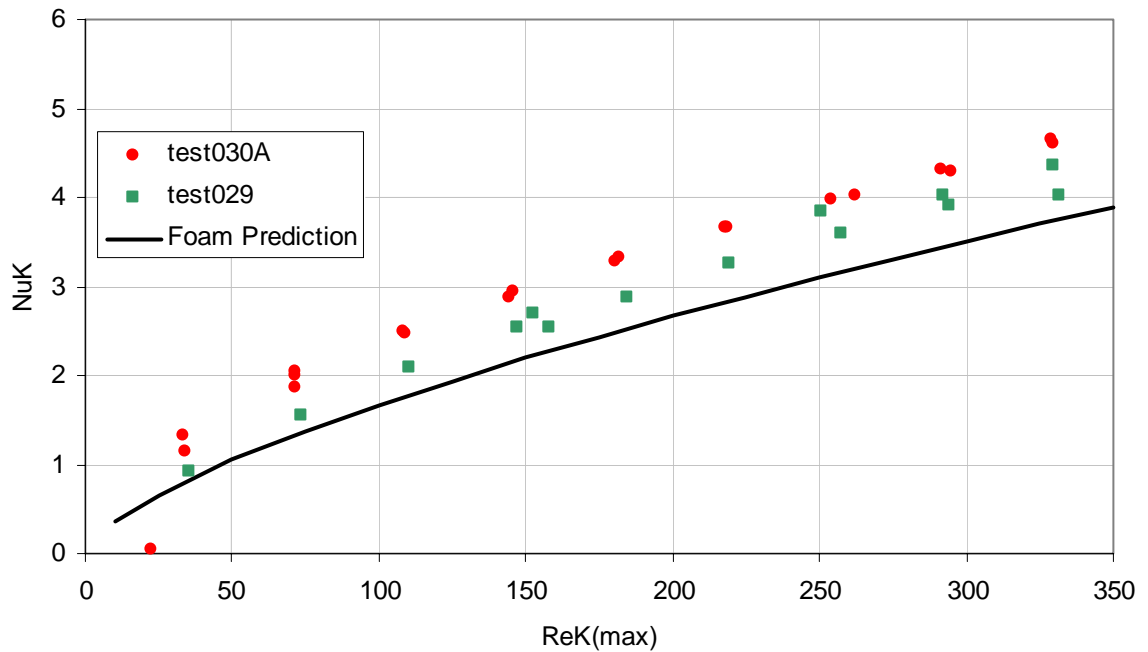


Figure 3.10 Heat transfer for 10ppi 5% (Nominal) SS single row sample tested at UTRC. Foam properties established by presure drop data.

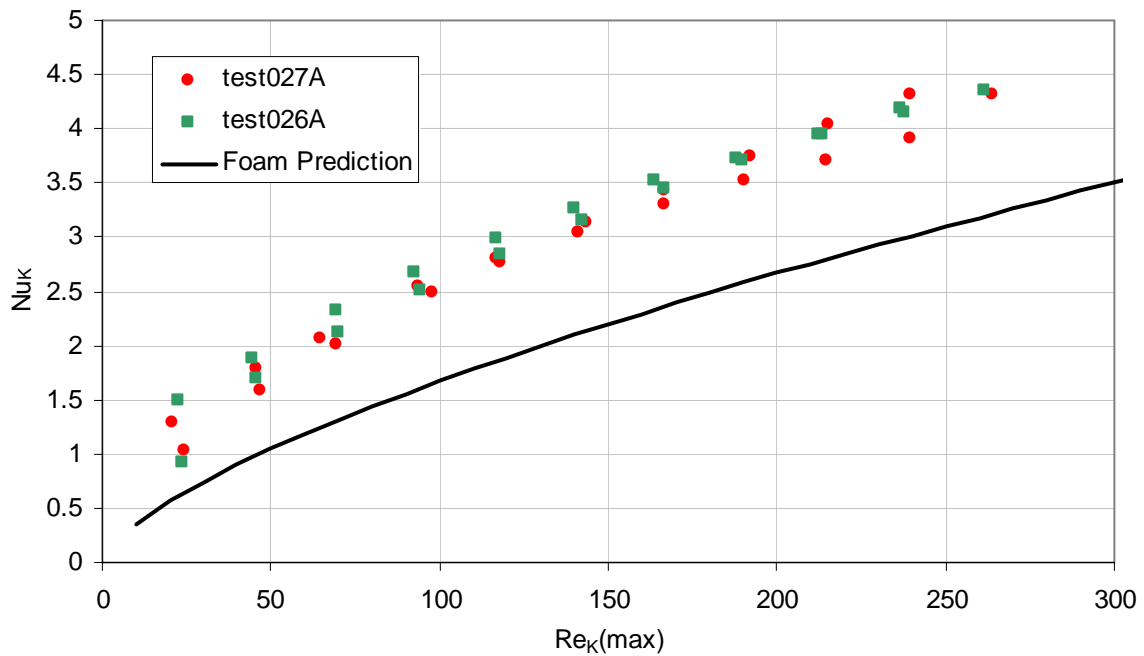


Figure 3.11 Heat transfer for 10ppi 5% (Nominal) Inconel single row sample tested at UTRC. Foam properties established by pressure drop data

All of the samples show heat transfer rates greater than that predicted by the foam-only relationship. The magnitude of the increase varies. However, each plot suggests that the increase is a constant shift rather than a multiplying factor. Figure 3.12 combines the data onto a single logarithmic plot. The Nu_K shift is between 0.2 and 1.5 above the foam-only prediction. This shift indicates that the tubes provide a mechanism to increase the heat transfer in the foam other than the simple increase in velocity due to blockage. This is expected as flow that impinges on the tubes will transfer heat in a way that is not captured by the foam-only model. The constant shift in the Nusselt number suggests that there would be heat transfer at a Reynolds number equal to zero. Such a condition is explained physically by natural convection around the tubes when there is no forced convection.

The 20ppi 10% (nominal) stainless steel brazed sample was also tested for heat transfer performance at HS Marston. The results are plotted in Figure 3.13. HS Marston's facility used hot oil in the tubes at various flow rates. The variation in the Nu_K for a given Re_K is a result of the variable oil flow. However, despite this variation, the data are consistent with that shown in Figure 3.12.

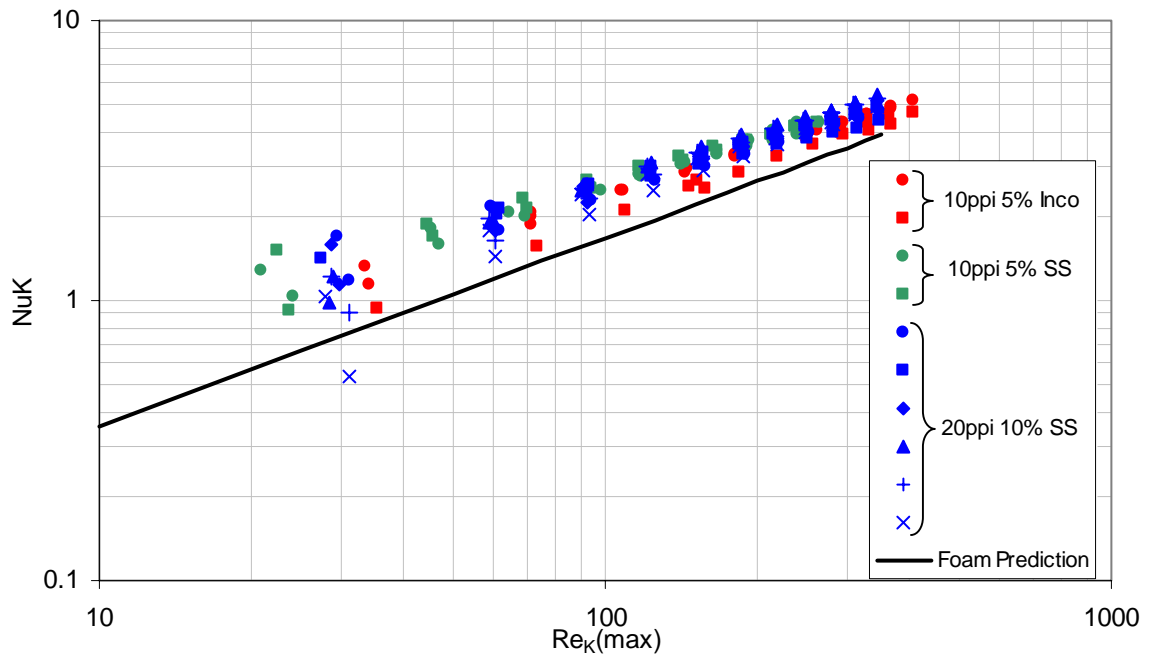


Figure 3.12 Summary of heat transfer data recorded for all single row samples at UTRC

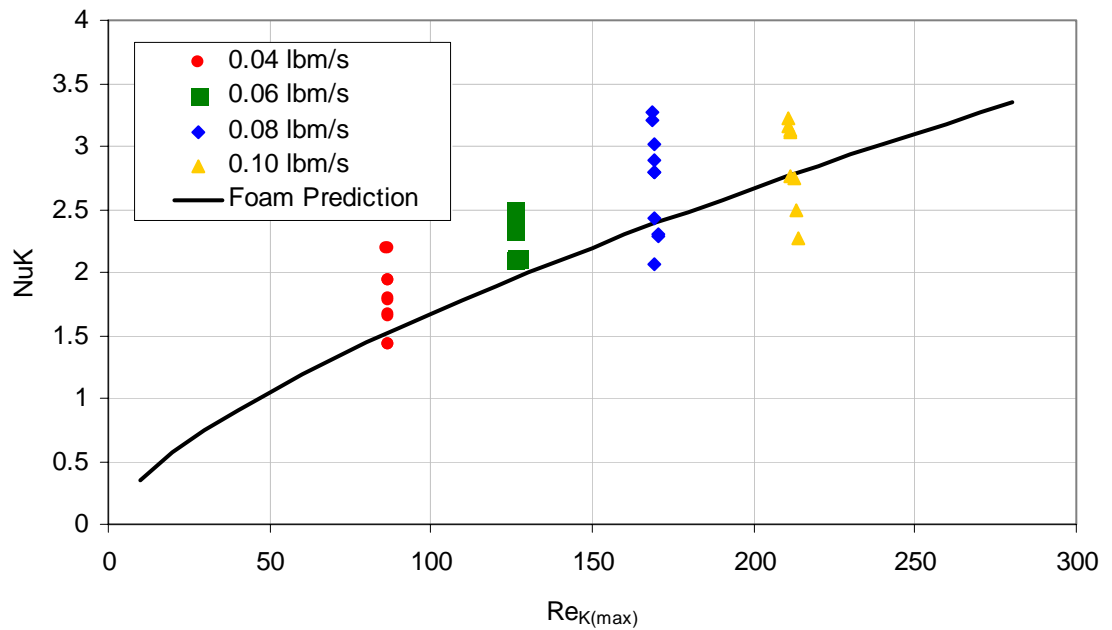


Figure 3.13 Heat transfer for 20ppi 10% (Nominal) Inconel single row sample tested at UTRC

3.3 Comparison to CFD model

Calimidi et al. (1999) proposed an effective-thermal-conductivity model to describe the heat transfer behavior of metal foam. The model considers the metal foam as a porous media and therefore the effective thermal conductivity is a weighted average of the air and metal foam conductivity:

$$k_{eff} = k_{foam}\phi + k_{air}(1 - \phi) \quad (3.9)$$

Using the commercially available Fluent porous media modeling package, the pressure drop and heat transfer for single-row samples were predicted. Figures 3.14 through 3.16 show the results as compared to the analytical predictions. The pressure drop was significantly under-predicted and the heat transfer was over-predicted when compared to both the analytical models and the data presented in Section 3.2. Although it is fully expected that the CFD model could be adjusted to better match the analytical predictions, the approach of the current study is to make direct use of the analytical predictions to estimate the metal foam/tube performance.

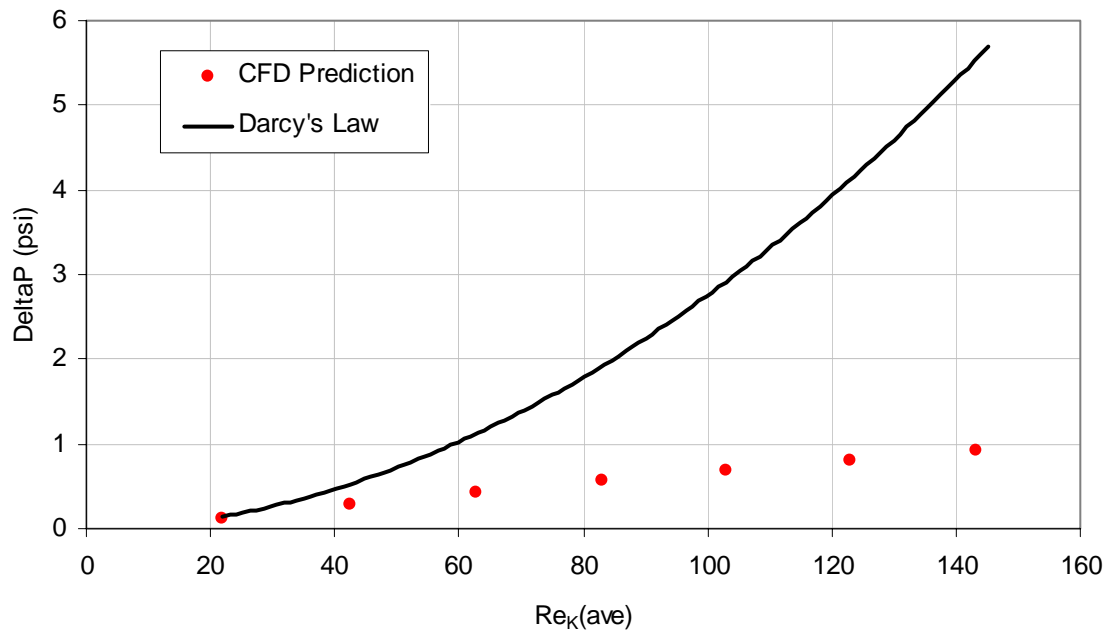


Figure 3.14 CFD predicted pressure drop for 20 ppi 10% SS single row sample

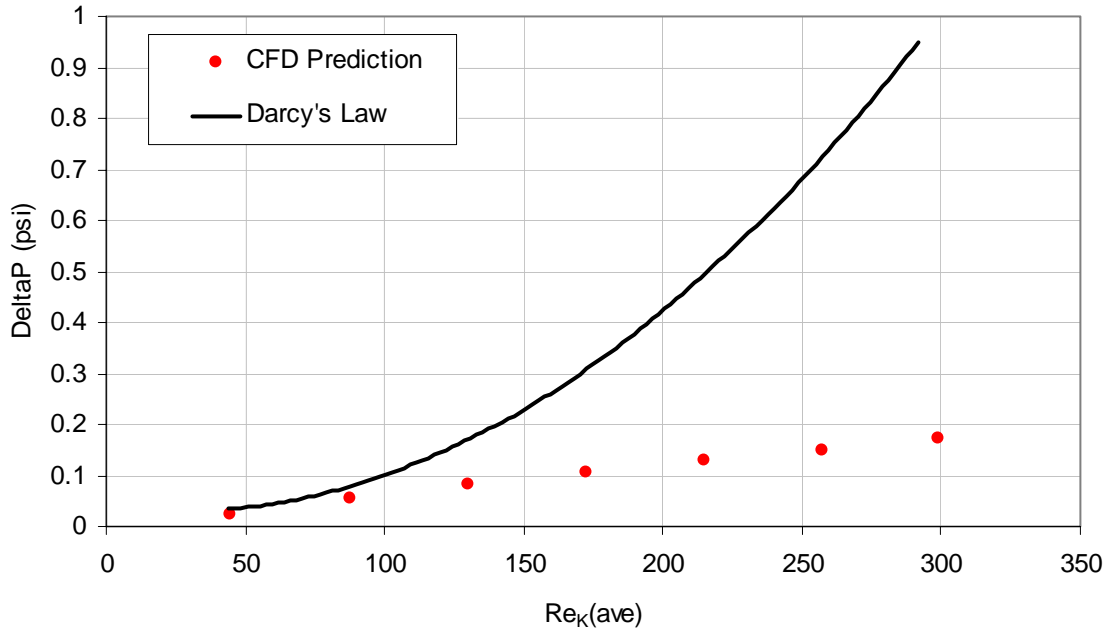


Figure 3.15 CFD predicted pressure drop for 10 ppi 5% SS single row sample

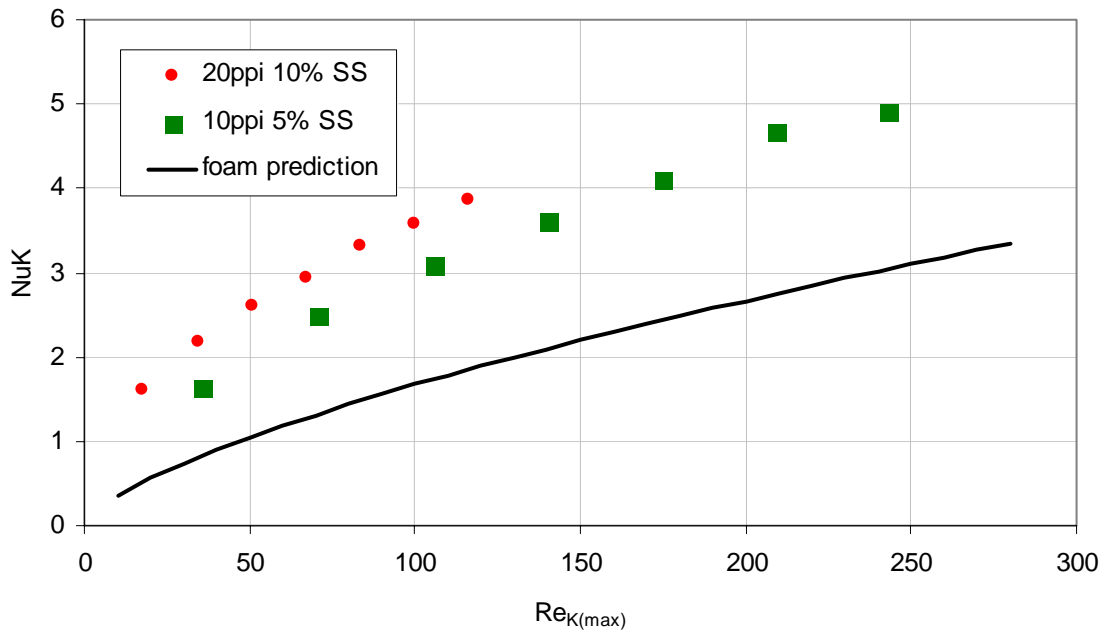


Figure 3.16 CFD predicted heat transfer for single row samples

3.4 Tube-Bank Experimental Results

The single tube row experiments presented in section 3.2 cannot be used to predict the behavior of foam around a staggered tube-bank. Therefore, fully three-dimensional tube-bank experiments were performed at HS Marston as described in Section 2.2. These experiments provided an opportunity to better calibrate and validate the pressure drop and heat transfer model presented in Section 3.1. Data were recorded for aligned and staggered tube-banks with and without metal foam (tube geometry shown in Figure 2.6).

Figures 3.17 and 3.18 show the heat transfer and pressure drop behavior recorded for the reference tube-bank samples in the form of the Colburn factor as a function of the Reynolds number. Note that the characteristic velocity and length scales are the inlet face velocity and the tube OD, respectively. The Reynolds number was based on these quantities to allow all of the tube-bank experiments to be easily compared. It can be seen that both the heat transfer and pressure drop are elevated compared to well known analytical predictions from Incropera and DeWitt (1990).

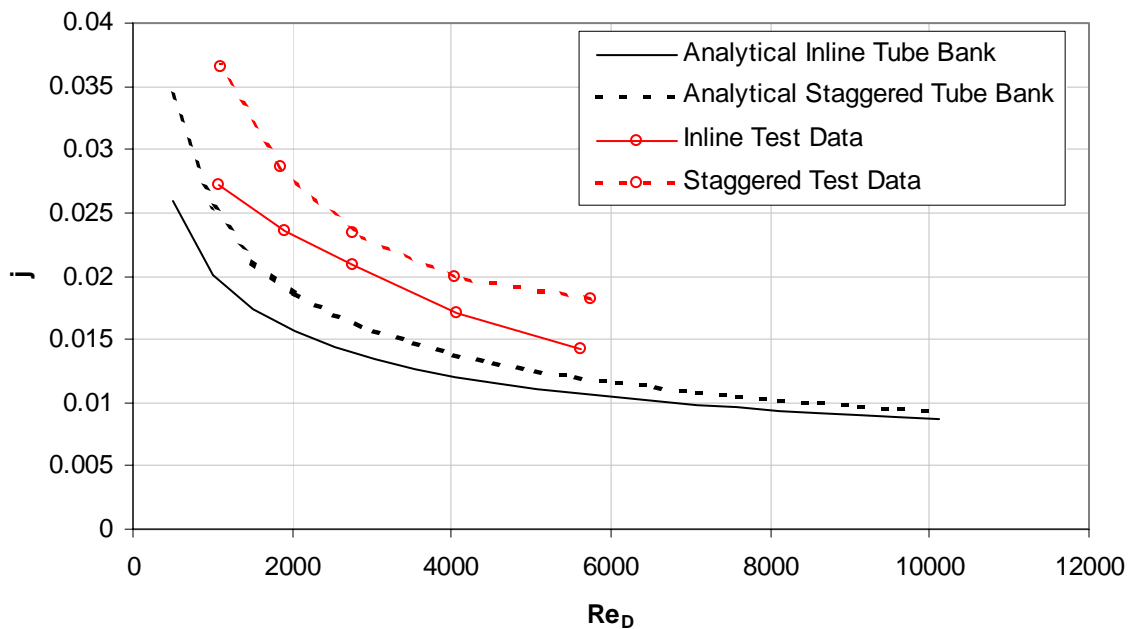


Figure 3.17 Heat transfer for reference tube-bank samples

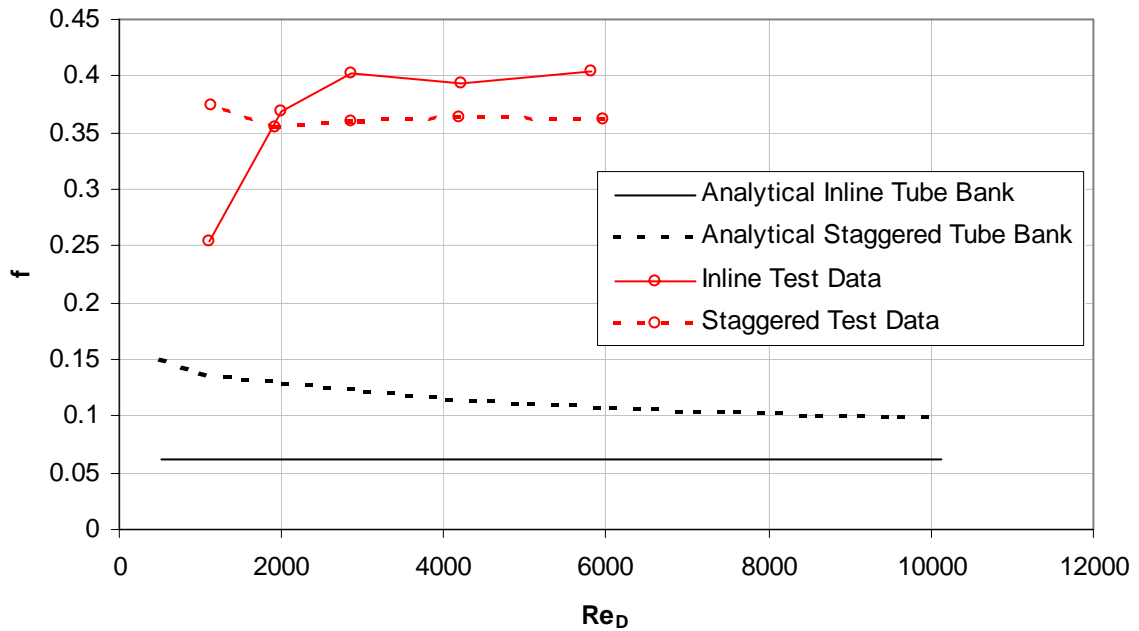


Figure 3.18 Friction factor for reference tube-bank samples

Stiffener plates (0.080 in. thick), required to keep the tube-banks from warping during the brazing process (Figure 3.19), may provide one explanation for the elevated pressure drop and heat transfer. The plates, acting as a fin, increase the skin friction and introduce some entrance losses.

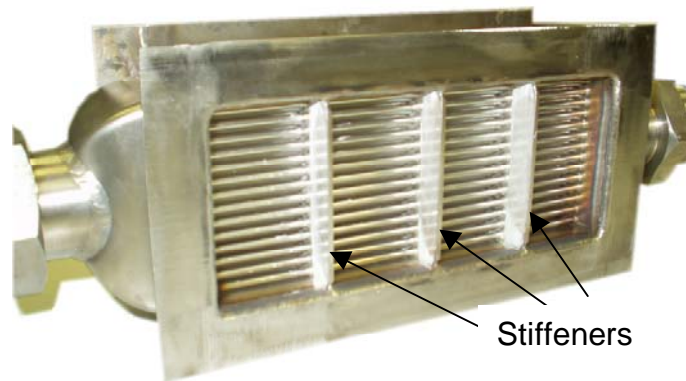


Figure 3.19 Reference tube-bank unit illustrating the stiffener plates required for manufacture.

Despite the overall shift in heat transfer, the relative behavior of the aligned and staggered tubes is expected. However, the friction factor shown in Figure 3.18 suggests an unexpected relationship in that the aligned tube-bank has a higher friction factor than the staggered tube-bank. During testing it was noted that the inline tube-bank generated significant acoustic vibration, a result of vortex shedding from upstream tubes interacting with downstream tubes. It is hypothesized that this acoustic resonance may be contributing to the increase pressure drop.

As the stiffener plates are not required or present in the metal foam samples and the acoustic resonance is also not present with the metal foam, the analytical baseline was selected as the reference for the metal foam units.

Figure 3.20 shows the heat transfer behavior of the aligned and staggered tube-banks with 25 ppi 5% 316 stainless steel foam brazed to the tubes. The largest pore size and lowest density foam was selected as dictated by manufacturing limits. The experimental data show that the staggered tubes have a significant impact on the heat transfer by increasing the Colburn factor 2.5X above a plain bank of tubes.

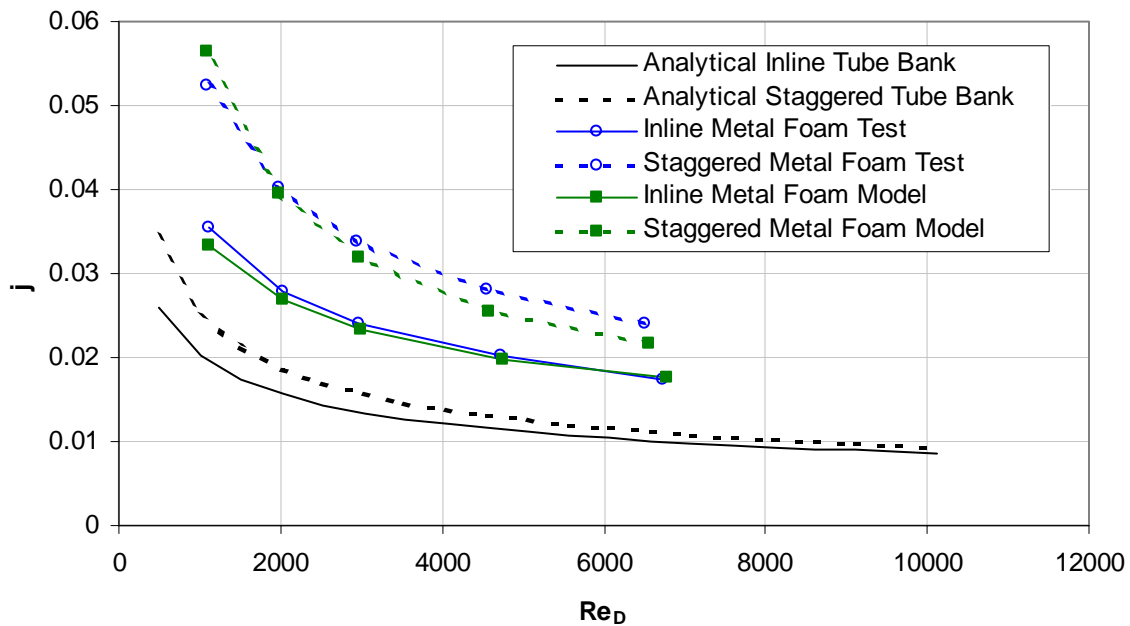


Figure 3.20 20ppi 5% SS metal foam tube-bank unit data with aligned and staggered tubes.

The analytical model predictions are from Equation 3.4 with a constant shift added to the Nusselt number to represent the impact of the tubes. A Nu_K shift of 0.2 was employed for the aligned tubes, while a shift of 2.0 was used for the staggered tubes. Figure 3.20 indicates that the analytical model is able to capture the magnitude and trend of the experimental data very well. The 0.2 shift is well within the expected range as measured with the single tube row data (Figure 3.12). Not surprisingly, the staggered tubes yielded a shift above the foam-only behavior larger than any of the single-row experiments.

Figure 3.21 shows the pressure drop behavior of the metal foam tube-bank samples as measured and predicted by Equation 3.5 used with the average Darcy velocity. The similar trends strongly suggest that the characteristic length scale of the foam dominates the flow behavior. Therefore the foam-only prediction is able to match the physical behavior of the foam/tube sample. As the foam dominates the pressure drop behavior, both the aligned and staggered tube samples have the sample pressure drop characteristic. Therefore, a staggered tube is clearly superior as it has enhanced heat transfer behavior with no increase in pressure drop.

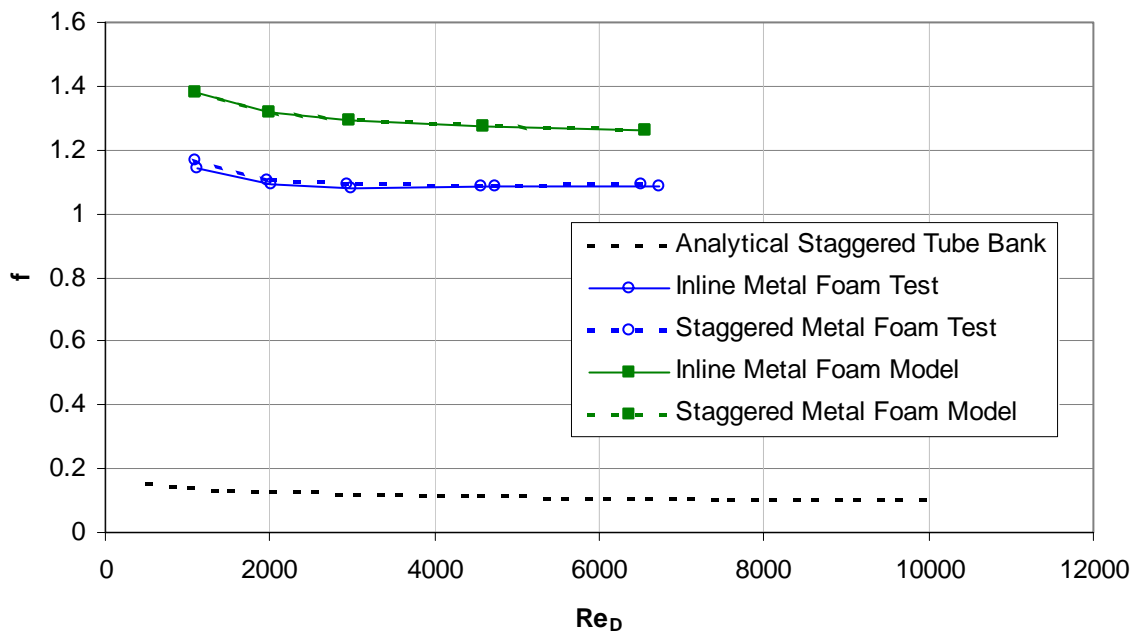


Figure 3.21 Reference tube-bank unit illustrating the stiffener plates required for manufacture.

Although the agreement between the magnitude of the data and prediction is reasonable, there is still a 20% difference. As discussed in Section 3.1, the pressure drop is extremely sensitive to the density of the foam. Therefore, no attempt was made to modify Equation 3.5 to better match experimental data.

3.5 Design Optimization

The analytical models calibrated to the tube-bank data in Section 3.4 were used to compare optimal metal foam designs to a conventional technology baseline for an advanced technology application. The application is representative of a cooled-cooling air heat exchanger with the requirements listed in Table 3.1.

Table 3.1 Full size heat exchanger application performance requirements

Fuel Side	
Flow rate:	13 lbm/min
Inlet pressure:	2000 psia
Inlet temperature:	230 F
Max. pressure drop:	100 psid
Air Side	
Flow rate:	17 lbm/min
Inlet pressure:	550 psia
Inlet temperature:	1250 F
Max. pressure drop:	25 psid
Outlet temperature:	550 F

Figure 3.22 shows the flow configurations considered for the optimization study. The baseline is a shell-tube heat exchanger with disc and donut baffles in which air is forced cross-flow through the tubes as it moves in a direction generally counter to the fuel flow. This is typical of conventional fuel/oil heat exchangers. As is also current convention, the baseline employs dimpled tubes to increase the heat transfer on the fuel side and minimize the size and weight.

Figure 3.22 also shows the metal foam configurations considered. The simplest implementation is a pure counter-flow heat exchanger shown in 3.22 (b). In this case, the airflow is parallel and counter to the fuel in the tubes and the foam dominates both the pressure drop and heat transfer behavior. To model this arrangement, the heat transfer is

assumed to be described by the foam only correlation in Equation 3.1 using the maximum velocity created by the tube blockage. The pressure drop is modeled with Equation 3.4 using the maximum Darcy velocity.

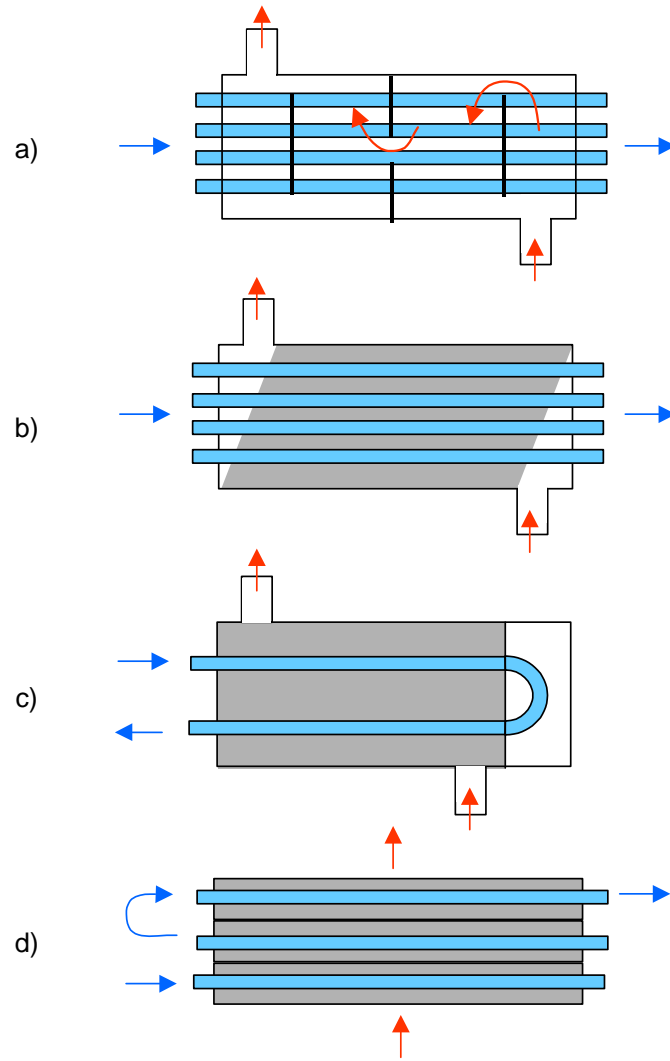


Figure 3.22 Heat exchanger flow configurations considered in the optimization of the metal foam design. a) Reference baffled cross-counterflow shell-tube. b) Counterflow metal foam. c) Cross u-tube metal foam. d) Cross flow (single/multiple passes).

Figure 3.22 (c) shows a cross-flow u-tube arrangement. This arrangement is typically used to allow the tubes to thermally expand without constraints to reduce stresses. Figure 3.22 (d) shows a purely cross-flow arrangement. Although this makes it simple to make multiple passes, the large flat separator plates required can have a significant impact on weight. Therefore, for this analysis, a single pass cross-flow arrangement was considered.

All of the cross-flow arrangements assume a staggered bank of tubes and employ the 2.0 shift in Nu_K as determined experimentally in Section 3.4. The optimization was executed with an in-house heat exchanger sizing program which optimizes the size and weight of a heat exchanger while meeting the performance requirements. This program was used to predict the reference shell-tube heat exchanger size and weight as well as that for the metal foam units. All units were design to meet the performance shown in Table 3.1.

The relationship between tube spacing and pore size was investigated to understand the optimal combination. The metal foam manufacturer recommends that at least two foam pores be present between the tubes to provide sufficient strength to capture the tubes. Because tube OD for this optimization study was selected to be the commonly used 0.094 in, the foam pore size essentially dictated by the tube spacing. This is because the largest pore size possible is most desirable to minimize the pressure drop, while maximizing heat transfer. Figure 3.23 shows how a cross-flow inconel metal foam heat exchanger weight changes with pore size for a 5% dense foam. The tube spacing for each case is twice the pore size.

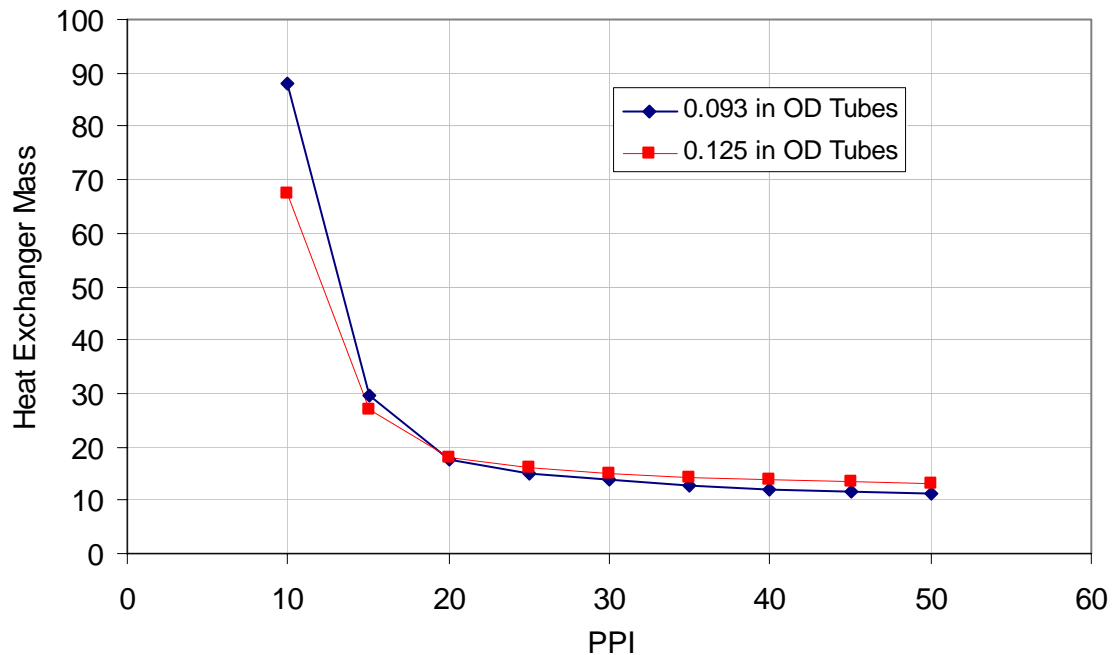


Figure 3.23 Heat exchanger mass as a function of pore size for both 0.093 and 0.125 in tubes for a cross-flow arrangement. The tube spacing is based on the manufacturing limit of two pores.

The figure indicates that the large tube spacing demanded by the larger pore foams (10 to 15 ppi) generates very large heat exchangers. As the pore size is reduced, the tube spacing can move closer and the heat exchanger gets smaller. However, the reduction in size is predominantly due to the increase in local velocity around the tubes as the space between the tubes gets smaller. This effect is experienced by a plain tube-bank. In fact, the figure suggests that as the heat exchanger gets smaller and the tubes get closer, the foam becomes less and less relevant. Figure 3.23 indicates that the same parametric study executed for 0.125 in. tubes produces very similar results.

Based on Figure 3.23, a 40 ppi 5% dense foam was used to evaluate the different flow configurations shown in Figure 3.22. Table 3.2 summarizes the heat exchanger designs for the baseline and different metal foam designs. Each heat exchanger meets the performance specified in Table 3.1. The comparison indicates that the both the counter and u-tube configuration are larger and heavier than the baseline two pass shell-tube design. The cross flow design has a similar weight and overall volume to the baseline, but has reduced the number of tubes by 40%. The results reflect that although the metal foam significantly augments the heat transfer, the pressure drop penalty balances the benefit.

Table 3.2 Optimal metal foam heat exchanger configurations vs. baseline shell-tube. All configurations have equivalent heat transfer performance.

Configuration	Tube spacing (%Tube OD)	Length (in)	Width (in)	Height (in)	Core Vol. (in ³)	Num. of Tubes	Mass (lbm)
Two Pass Shell Tube	30%	6.5	3	3	60	550	7
Counter Flow Foam	50%	10	3	3	90	550	12
Cross U-Tube Foam	50%	8	5	3	120	650	14
Cross Flow Foam	50%	7	11	1	77	350	8

4.0 Cellular Metal Results

4.1 Cellular Metal Tube-Bank Experimental and CFD Results

Two cellular metal tube-bank samples were fabricated and tested. Figures 4.1 and 4.2 show the periodic arrangement of the hollow-truss samples. The figures show the tubes which contain liquid in dark gray and hollow rods that strengthen the matrix, but do not convey liquid, in light gray. In both figures, the tubes are aligned and the rods are staggered. The tube arrangement is identical to the aligned tube bank baseline unit. The pitch of rods in the dense design is exactly twice that of the open design. As with the baseline, all tubes have a 0.094 in. OD and both tubes and rods have a wall thickness of 0.007 in.

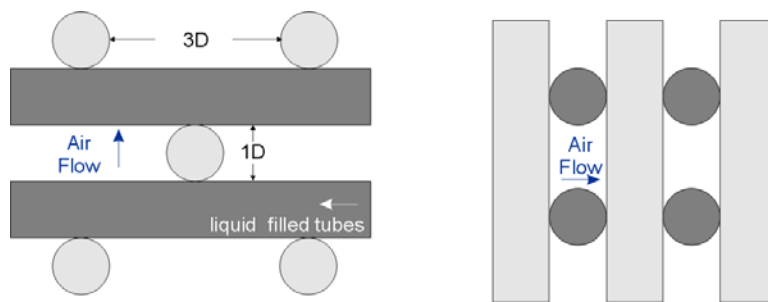


Figure 4.1 Top and side view of open cellular metal configuration.

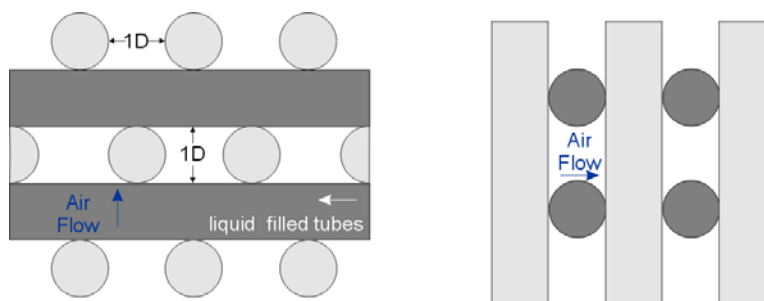


Figure 4.2 Top and side view of dense cellular metal configuration.

CFD was employed to calculate the performance of the test units and extend the design space to configurations that could not be experimentally tested in the current study. CFD is well suited for the analysis of cellular metal as it directly models the principal behavior of the fluid which generates the heat transfer; flow around the tubes. In contrast, the metal

foam CFD analysis employed a bulk approximation that does not directly model the fundamental fluid/foam behavior and therefore does not necessarily predict the heat transfer even when applied over a fine mesh. The additional designs considered with CFD are shown in Figures 4.3 through 4.5 below. The computational domain for the 3-D CFD analysis was defined as the smallest periodic element. Periodic inlet and outlet conditions were assumed and the grid was generated with sufficient resolution to calculate the boundary layer behavior without wall functions. The performance of the single periodic element was directly scaled to predict the performance of the entire tube-bank sample so the experimental data could be directly compared to the CFD results. The complete CFD results set is included in Appendix 7.4.

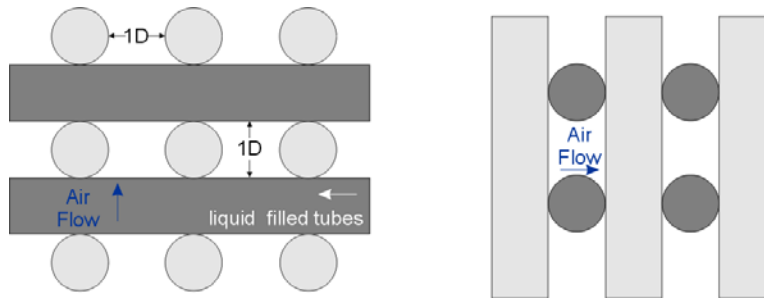


Figure 4.3 Top and side view of dense aligned cellular metal configuration.

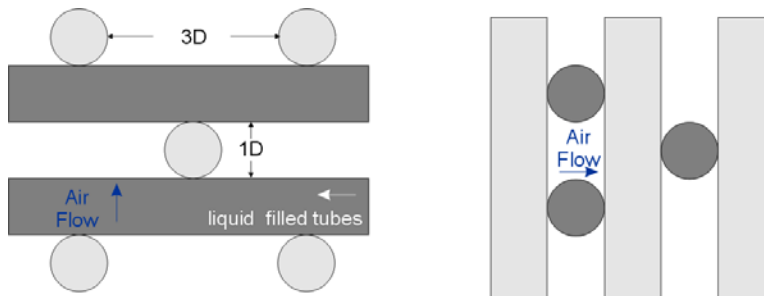


Figure 4.4 Top and side view of open staggered cellular metal configuration.

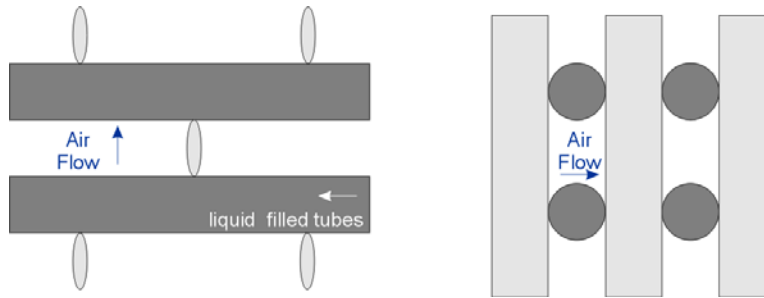


Figure 4.5 Top and side view of open elliptical cellular metal configuration.

Experimental data and CFD predictions for the open and dense configurations are shown in Figure 4.6. For reference, the CFD predicted performance of the aligned baseline configuration is also included in the Figure. It can be seen that the CFD reasonably predicts the experimentally measured performance of the tube-bank test samples. Note that the CFD over predicts the performance of the aligned tube-bank reference as compared to the analytical relationship, but this is very similar to the aligned tube-bank experimental performance shown in Figure 3.17. Therefore it is concluded that the CFD heat transfer predictions are reasonable and can be used to make relative comparisons.

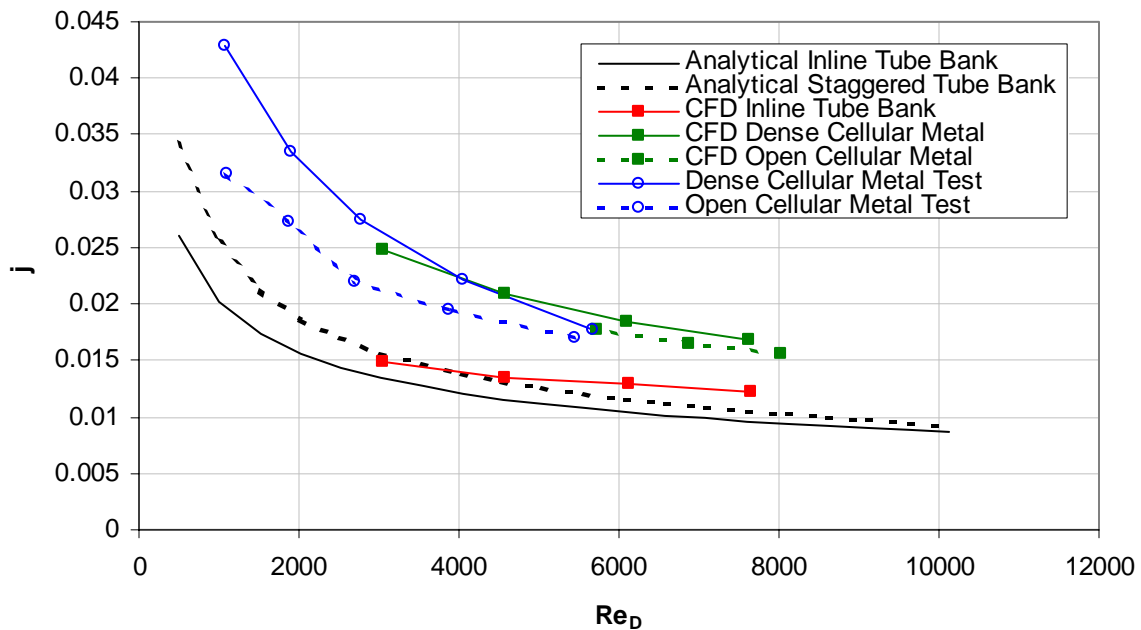


Figure 4.6 Comparison of cellular metal experimental and CFD predicted heat transfer performance.

Figure 4.7 shows the pressure drop test results and CFD predictions for the open and dense cellular metal tube-bank samples. Unlike the heat transfer performance, there are significant discrepancies between the measured and predicted pressure drop. First examining the experimental data, the dense configuration shows an expected trend that is smooth with Reynolds number. However the open configuration shows significant variation with Reynolds number. It is believed that this variation is a result of the large acoustic flow induced vibration generated by the air passing through the cellular metal matrix. This is the same phenomenon observed during the testing of the aligned tube-bank reference sample.

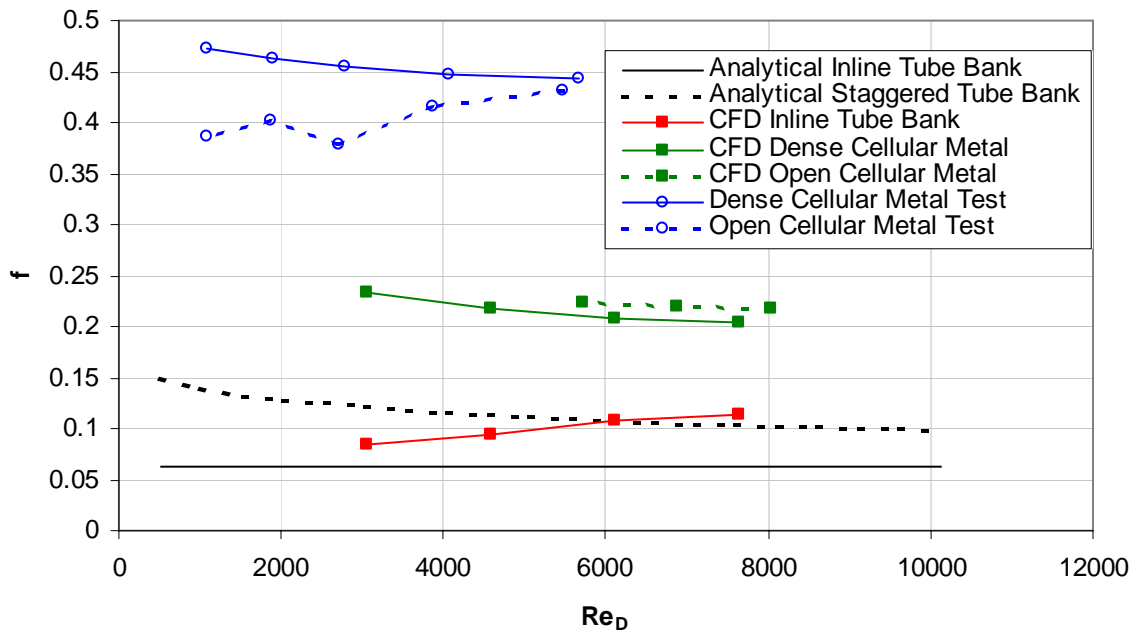


Figure 4.7 Comparison of cellular metal experimental and CFD predicted friction factor.

Figure 4.8 shows a direct comparison of the cellular metal and reference tube-bank sample friction factor data. The data suggest that the dense cellular metal friction factor is approximately 25% greater than that for the staggered tube-bank. Because the cellular metal samples would have similar flow behavior to the plain tube-bank, unlike the metal foam, it is proposed that it is reasonable to compare the experimental cellular metal results to the experimental baseline. Because of the large variation in the open cellular sample data and the presence of such large acoustic vibrations, no specific conclusion is drawn from the data.

To examine the CFD results more closely, Figure 4.9 plots the CFD predictions for the cellular metal samples with the analytical predictions. In Figure 4.9, however, the CFD results have been uniformly scaled so that the CFD prediction of the plain aligned tube-bank most closely matches the analytical model. The figure shows that scaled CFD cellular metal predictions are approximately 25% greater than the staggered analytical model. It is therefore concluded that the scaled CFD pressure drop results can be used to make comparisons between different cellular metal designs.

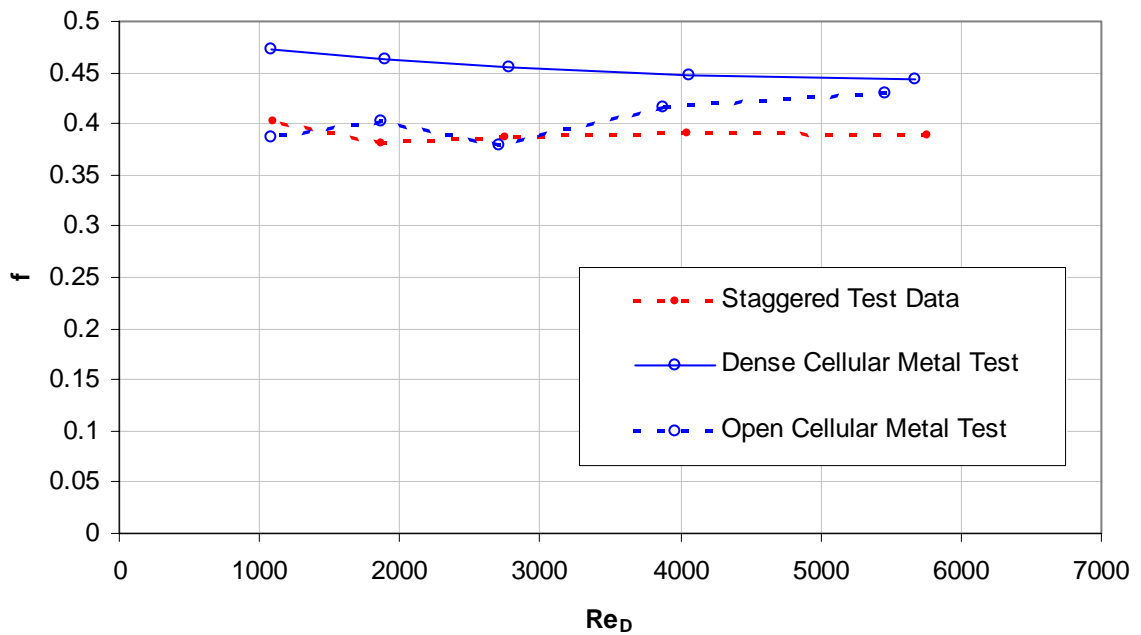


Figure 4.8 Comparison of cellular metal measured friction factor to the reference staggered tube sample.

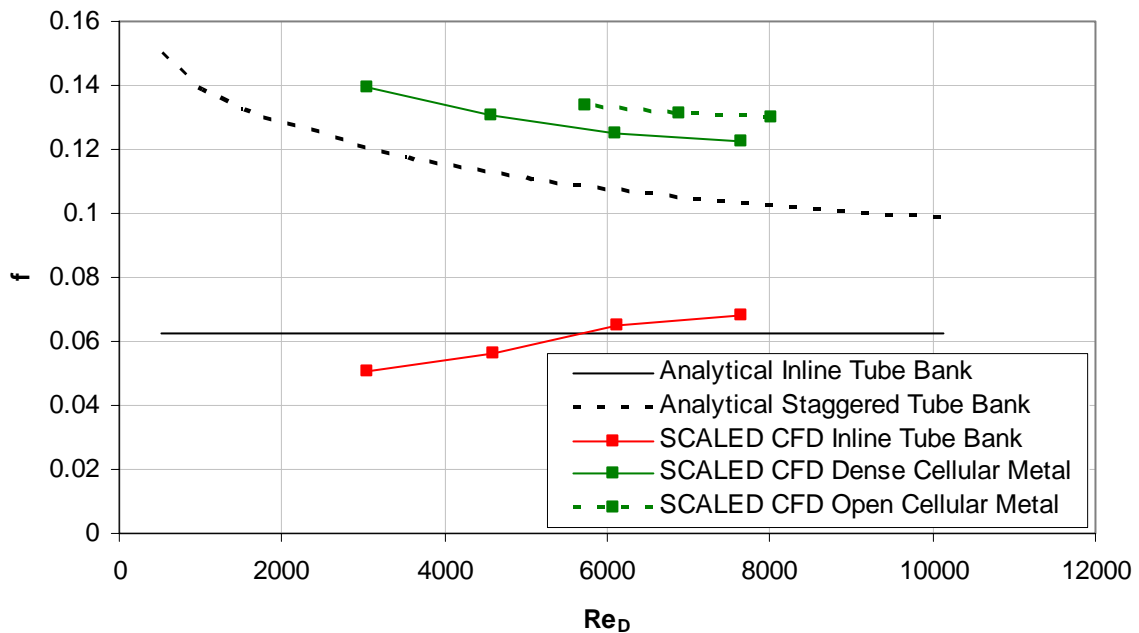


Figure 4.9 CFD predictions for cellular metal tube-bank samples that have been uniformly scaled such that the the aligned tube-bank predictions closely match the analytical model.

Using the calibration described above, the alternate cellular metal geometries shown in Figures 4.2 through 4.5 were compared to the performance of the units tested. Figure 4.10 shows the comparison of the heat transfer performance. The dense inline rod arrangement has an obvious loss of performance. This is not surprising, as when the rods are aligned, the wakes of the upstream rods make the heat transfer of the downstream rod less effective. The variations of the open cellular design appear to have small impact on the heat transfer.

Examining the scaled pressure drop in Figure 4.11 shows that the dense inline rod arrangement produces an increase in pressure drop. This configuration produces less heat transfer and higher pressure drop and is clearly undesirable. However, the open elliptical design showed similar heat transfer to the open cellular configuration with round rods, but Figure 4.11 shows that it has a friction factor similar to a plain staggered tube bank. This is the most promising result of all the configurations modeled.

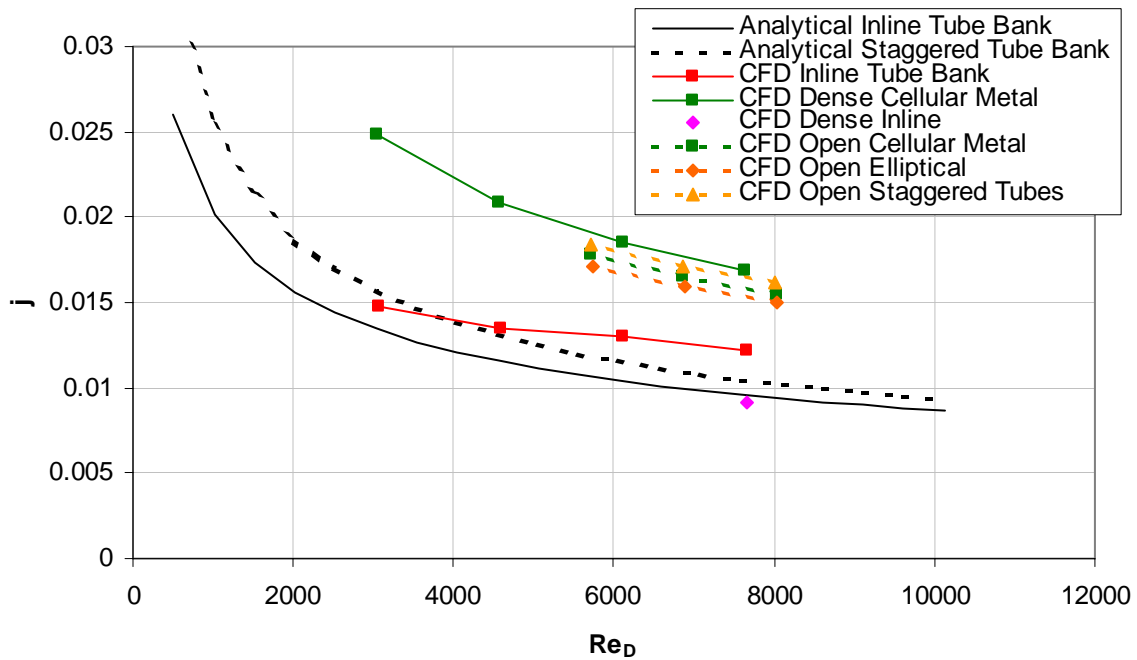


Figure 4.10 CFD predictions of heat transfer performance for different cellular metal configurations

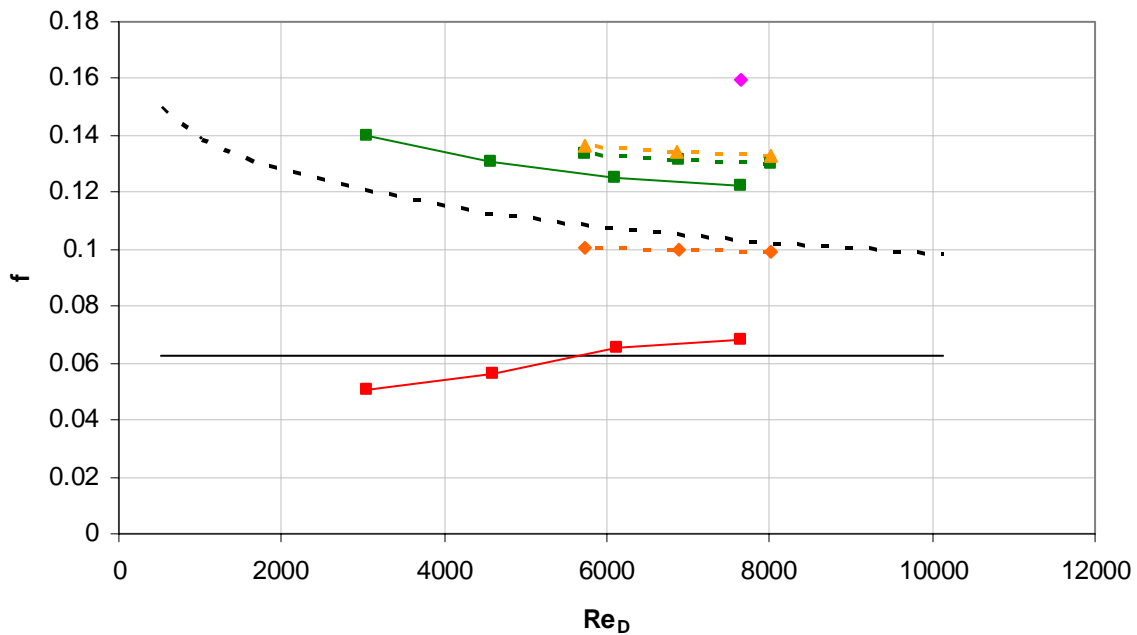


Figure 4.11 Scaled CFD predictions of pressure drop behavior in cellular metal as compared to analytical models of plain tube banks.

To understand the mechanism that allows the elliptical rod configuration to improve the performance so significantly, the local surface heat transfer coefficient for the round and elliptical rod configurations as calculated with CFD is shown in Figures 4.12 and 4.13. Both plots use identical scales so they can be directly compared. It can be seen that the heat transfer coefficient is increased at the leading edge of the elliptical rods as compared to the round rods. This is due to the smaller wakes of the rods immediately upstream due to the low-loss elliptical shape. Additionally, the surface velocity near the rods is higher as the wakes are contained to a smaller region.

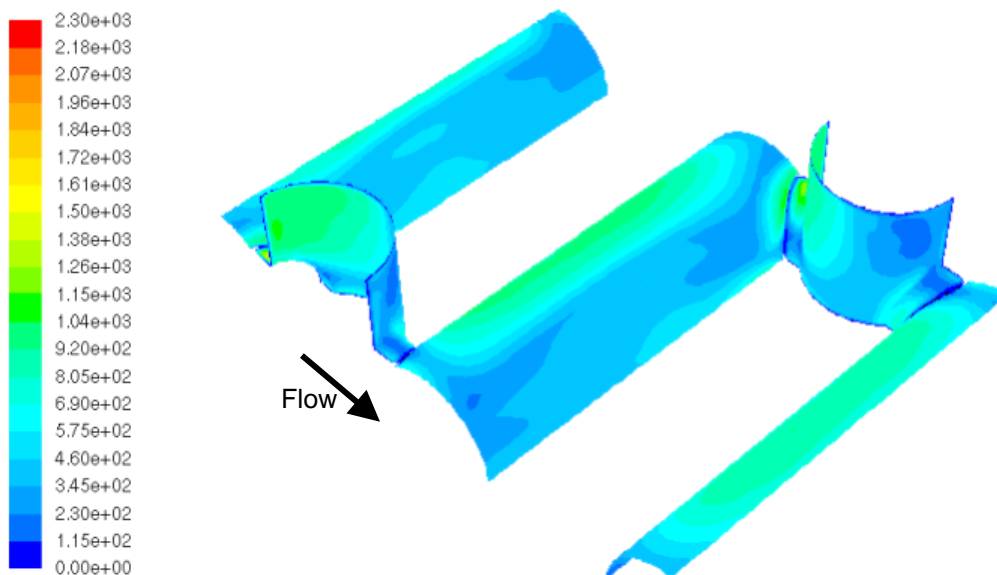


Figure 4.12 CFD calculated heat transfer coefficient ($\text{W}/\text{m}^2/\text{K}$) for the open cellular metal configuration.

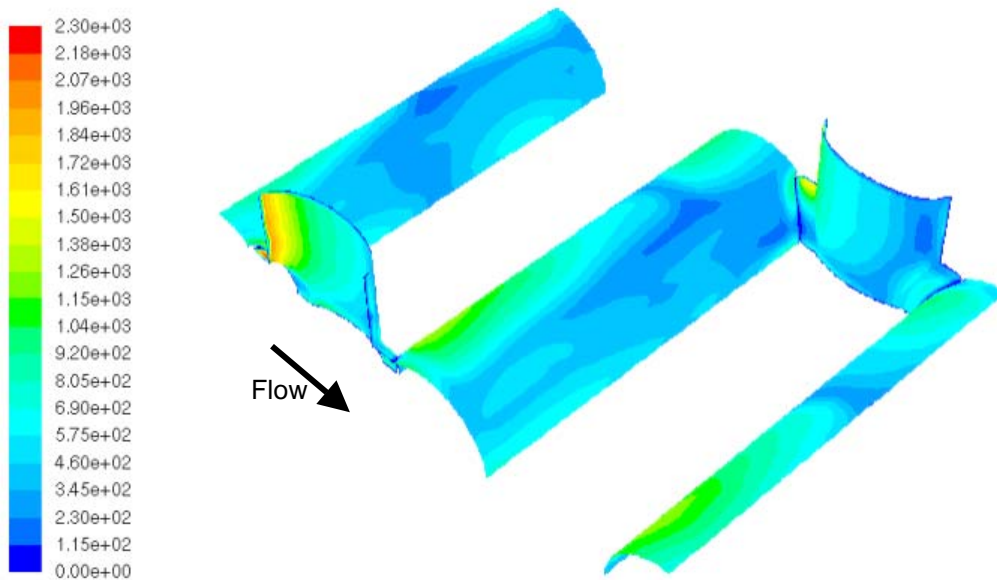


Figure 4.13 CFD calculated heat transfer coefficient ($W/m^2/K$) for the open cellular metal with elliptical rods (4:1 aspect ratio).

Based on these results, a performance model for the hollow-truss cellular metal with elliptical rods is proposed in which the heat transfer is the same as that for a staggered bank of tubes with the same tube spacing, but has a 50% increase in Colburn factor, j . It is this model that will be used in the following section in which an optimal design will be compared to a conventional baseline in a practical cooled-cooling air application.

4.2 Cellular Metal Design Optimization

With the model developed in the previous section, the open cellular metal with elliptical rods was compared to a traditional shell-tube heat exchanger for the application described in Section 3.5. The elliptical configuration was selected because it offered the best performance with the smallest pressure drop increase. Additionally, the open configuration adds less weight than the dense configurations. The optimization was carried out with the same heat exchanger sizing program employed in the optimization of the metal foam design in Section 3.5. As with the metal foam, dimpled tubes are used to provide as much heat transfer on the liquid side as possible.

In an effort to identify the optimal configuration, the cellular metal tube spacing was varied and the impact on the size and weight recorded. The results of the parametric study are listed in Table 4.1. Note that for the open configuration, the weight of the rods is 20% of the plain bank of tubes. The table shows that when the rods and tubes are the same size (100% tube spacing) there is no size or weight benefit. Despite the improved heat transfer over staggered tubes with the same tube spacing, the cellular metal improvement is negated when compared to plain tubes with a spacing smaller than 100% of a tube OD, as is often the case in conventional shell-tube units

Table 4.1 Open cellular metal configuraiton with elliptical rods compared to conventional shell-tube heat exchanger for Table 3.1 conditions. All configurations have equivalent heat transfer performance.

Configuration	Tube spacing (%TubeOD)	Length (in)	Width (in)	Height (in)	Core Vol. (in ³)	Num. of Tubes	Mass (lbm)
2 Pass Shell Tube	30%	6.5	3	3	60	550	7
2 Pass Cellular	30%	2	2	7.5	30	300	5.5
2 Pass Cellular	40%	2.5	2.5	7	44	400	6.5
2 Pass Cellular	50%	3	3	7	63	450	7.5
2 Pass Cellular	100%	5	5	6.5	163	750	12

Table 4.1 also shows the size and weight for elliptical cellular metal configurations with a tube spacing smaller than 100% of the tube OD. Figure 4.14 illustrates that one way to manufacture such a cellular metal configuration is to dimple the rods to allow them to receive the tubes. This increases the complexity of manufacture, but may actually have a heat transfer benefit as the contact area between the tubes and rods will be increased. No such benefit was included in the current results. An alternative manufacturing technique would be to use smaller diameter elliptical rods. However, it is assumed that dimpled rods would have performance most similar to the model proposed and while smaller and smaller diameter rods would have a decreasing impact on the flow field and most likely less benefit.

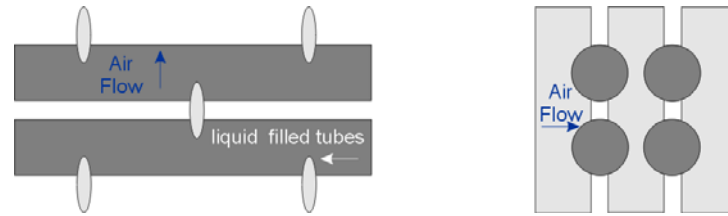


Figure 4.14 Top and side view of open cellular metal configuration with elliptical rods. Tube spacing is 30% of tube OD.

Table 4.1 indicates that cellular metal is projected to have a benefit with tube spacings of 30-40%. Both configurations suggest a volume and weight benefit and a reduction in the number of tubes, which may be a reliability benefit. It is important to note that the structural integrity of the heat exchanger is not considered in this analysis, but Wadley et al. (2003) determined that hollow truss construction was superior to both metal foam and honeycomb construction under bending and compressive loads.

5.0 Summary and Conclusions

Tubular metal foam and hollow-truss cellular metal heat exchangers were examined for performance, size and weight benefits relative to conventional shell-tube technology. To estimate performance, an analytical model for a tubular metal foam heat exchanger was calibrated to experiments. The heat transfer model is based on a power-law relationship between the Nusselt number and the Reynolds number in which the permeability of the foam is used as the characteristic length scale. When the foam is used to augment the heat transfer of a tube-bank, the foam-only Nusselt number power-law relationship is shifted by a constant (the constant being established experimentally for aligned and staggered tubes). The data show that when metal foam is used with a staggered bank of tubes the heat transfer is 40 percent higher than when foam is used with an aligned bank. This is due to the increased contribution of the flow impinging on the tubes. The data also indicates that the metal foam dominates the pressure drop through the foam and tubes. The analytical heat transfer and pressure drop model was used to predict the performance of cross-flow, counter-flow, and u-tube metal foam heat exchangers for a fuel/air heat exchanger in a cooled-cooling air (CCA) application.

The CCA application constrains the tube diameter due to the high fuel pressures present in the fuel system. Additionally, the minimum tube spacing is dictated by the pore size of the metal foam, as tubes placed closer than two pores would have few ligaments between them for support. With these constraints, it was not possible to find a foam/tube spacing combination that would provide a weight or size benefit when compared to a conventional technology shell-tube heat exchanger with equivalent performance. A cross-flow configuration was identified which may reduce the number of tubes as compared to the baseline, resulting in a potential reliability benefit.

Hollow-truss cellular metal was also investigated as an improved heat exchanger core material for the same CCA application. Based on CFD and experimental results, the best projected performance is obtained with nonflowing elliptical rods placed in a sparse staggered arrangement in an aligned bank of tubes which flow liquid. The elliptical rods provide the lowest additional pressure drop while still creating turbulence and creating more surface area for stagnation heat transfer. It is projected that such a configuration can produce more than a 10% reduction in weight and 30% reduction in volume. However,

R05-5.300.0022

these benefits require the rods be dimpled or otherwise modified so the tubes can be spaced closer than one diameter. The feasibility of the manufacturing process required to fabricate a cellular metal matrix with dimpled elliptical hollow-rods was not investigated, but it will be significantly more complex than the process for a conventional shell-tube heat exchanger.

6.0 References

- Calmidi, V. V., 1998, "Transport Phenomena in High Porosity Fibrous Metal Foams," Ph. D. Dissertation, University of Colorado.
- Calmidi, V.V. and Mahajan R.L., 1999, "The Effective Thermal Conductivity of High Porosity Fibrous Metal Foam," *Journal of Heat Transfer*, Vol 121, pp.466-471.
- Floyd, Donald, 2001, "Fluid Properties of Open Cell Sintered Iron Based Porous Metal Structures", Porvair Fuel Cell Technology Report.
- Haack, D.P., Butcher, K.R., Kim, T. and Lu., T.J., 2001, "Novel Lightweight Metal Foam Heat Exchangers," ASME Mechanical Engineering Conference.
- Hunt, M.L. and Tien C.L., 1988, "Effects of Thermal Dispersion on Forced Convection in Fibrous Media," *International Journal of Heat and Mass Transfer*, Vol 31, pp. 301-309.
- Incropera, Frank P. and DeWitt David P., 1990, *Fundamentals of Heat and Mass Transfer*. 3rd ed. New York: John Wiley and Sons.
- Queheillat, D.T. and Wadley, H.N.G., 2004, "Cellular metal lattices with hollow trusses," *Acta Materialia*, Vol 53, pp. 303-313.
- Sabatino D., Spadaccini L., Chiappetta, L. and Huang, H., 2004, "Compact Lightweight Heat Exchanger for Turbine Thermal Management," UTRC Report R04-6.100.0008-6
- Wadley, H.N.G, Fleck, N.A and Evans, A.G., 2003, "Fabrication and Structural Performance of Periodic Cellular Metal Sandwich Structures," *Composites Science and Technology*, Vol 63, pp. 2331-2343.

7.0 Appendix

7.1 Single Tube-Row Metal Foam Experimental Data (UTRC)

Table 7.1 Metal Foam UTRC Test 9 Data

Mass Flow lbm/s	ReK -	Inlet Temp F	Outlet Temp F	ΔP psi
0.005	12.25	72.80	72.54	0.034
0.005	12.11	72.92	118.19	0.037
0.005	12.05	72.89	129.67	0.037
0.010	23.52	72.02	131.95	0.086
0.020	46.37	71.12	122.91	0.210
0.030	68.73	70.91	119.63	0.337
0.040	91.90	70.18	116.26	0.469
0.050	115.33	69.21	112.67	0.597
0.060	139.36	68.13	108.99	0.723
0.070	162.62	67.91	106.64	0.845
0.080	186.34	67.93	104.51	0.967
0.090	210.10	67.38	103.59	1.096
0.100	234.11	67.33	102.32	1.216
0.110	257.17	67.18	101.72	1.332
0.099	231.41	67.57	103.86	1.211
0.089	207.69	68.27	106.46	1.100
0.079	183.98	69.18	112.12	0.986
0.070	161.23	70.23	116.19	0.873
0.059	136.46	71.49	120.87	0.753
0.049	113.16	73.50	128.10	0.629
0.039	89.84	74.63	132.56	0.496
0.030	67.23	76.62	142.70	0.355
0.019	43.35	80.02	157.06	0.200
0.010	21.60	85.69	177.19	0.061
0.010	22.09	87.52	134.72	0.055

Table 7.2 Metal Foam UTRC Test 10 Data

Mass Flow lbm/s	ReK -	Inlet Temp F	Outlet Temp F	ΔP psi
0.010	22.64	90.33	181.35	0.076
0.011	23.03	89.99	185.71	0.077
0.020	44.28	84.91	168.12	0.214
0.040	89.41	80.46	149.94	0.488
0.040	90.02	79.81	147.70	0.488
0.050	113.47	78.38	138.95	0.608

R05-5.300.0022

0.060	136.78	77.67	130.43	0.735
0.070	158.82	77.05	125.77	0.862
0.080	184.25	76.57	115.86	1.015
0.090	206.68	75.31	117.42	1.143
0.099	229.13	74.37	115.32	1.284
0.101	232.68	73.92	114.69	1.332
0.100	230.93	73.94	109.28	1.319
0.089	205.97	73.52	111.54	1.193
0.079	180.81	74.05	120.41	1.068
0.080	182.46	73.78	123.67	1.070
0.080	183.39	73.85	125.31	1.069
0.100	229.20	73.32	120.25	1.310
0.109	251.94	73.01	117.89	1.432
0.099	228.45	73.20	119.66	1.299
0.089	204.95	73.63	122.49	1.160
0.079	181.35	74.30	126.47	1.015
0.059	135.08	76.22	133.53	0.732
0.049	111.74	77.55	139.74	0.586
0.039	88.63	79.54	146.48	0.439
0.028	61.80	81.86	154.66	0.266
0.020	44.68	83.88	163.31	0.164

Table 7.3 Metal Foam UTRC Test 11 Data

Mass Flow lbm/s	ReK -	Inlet Temp F	Outlet Temp F	ΔP psi
0.109	255.67	69.25	99.39	1.239
0.110	257.40	67.83	101.42	1.276
0.099	232.49	66.28	102.75	1.198
0.090	209.32	66.20	105.76	1.116
0.079	185.03	66.66	109.74	1.022
0.069	161.07	67.67	113.18	0.919
0.059	136.74	68.38	117.04	0.802
0.049	113.83	69.96	122.54	0.678
0.040	90.38	72.18	130.11	0.538
0.030	66.88	74.86	141.20	0.384
0.019	43.54	78.21	157.38	0.219
0.010	21.42	84.41	182.76	0.058

Table 7.4 Metal Foam UTRC Test 12 Data

Mass Flow lbm/s	ReK -	Inlet Temp F	Outlet Temp F	ΔP psi
0.010	22.94	71.67	125.25	0.078

R05-5.300.0022

0.020	44.66	69.24	140.54	0.176
0.030	68.66	68.01	134.16	0.295
0.040	91.78	67.59	129.30	0.411
0.050	114.96	67.73	125.91	0.528
0.060	138.22	67.69	122.79	0.643
0.070	161.12	68.06	120.50	0.756
0.080	183.78	68.32	118.65	0.871
0.090	207.90	68.36	116.73	0.991
0.100	231.20	68.49	115.89	1.109
0.110	254.85	68.35	114.01	1.225
0.099	229.64	68.67	116.31	1.127
0.089	205.94	69.23	118.78	1.031
0.079	182.86	69.87	121.82	0.927
0.069	159.37	70.65	125.90	0.820
0.060	136.04	71.55	130.63	0.709
0.049	112.47	72.70	136.46	0.583
0.039	89.05	74.07	144.02	0.452
0.030	66.28	75.90	153.30	0.326
0.020	43.63	78.02	163.54	0.193
0.009	20.64	82.13	180.00	0.058

Table 7.5 Metal Foam UTRC Test 13 Data

Mass Flow lbm/s	ReK -	Inlet Temp F	Outlet Temp F	ΔP psi
0.010	23.02	74.85	122.78	0.093
0.010	22.63	73.39	148.54	0.094
0.010	22.93	72.96	156.99	0.097
0.020	44.57	72.01	151.84	0.217
0.030	68.58	71.21	145.15	0.358
0.040	91.44	71.11	139.70	0.493
0.050	114.48	71.25	135.34	0.620
0.060	136.56	71.41	131.80	0.737
0.070	160.54	71.21	128.60	0.860
0.080	183.44	71.35	126.01	0.978
0.090	206.69	71.46	123.48	1.094
0.100	229.91	71.38	121.38	1.208
0.110	253.30	70.10	118.10	1.319
0.099	228.69	69.73	119.72	1.195
0.089	205.63	69.61	122.13	1.078
0.079	182.22	69.88	125.24	0.961
0.069	159.04	69.72	128.45	0.843
0.060	136.15	70.19	132.67	0.726
0.049	112.55	71.03	138.14	0.605
0.039	89.22	72.22	144.79	0.478
0.030	66.55	74.62	154.36	0.346
0.020	43.47	78.02	167.05	0.201
0.010	21.12	84.43	188.81	0.064

Table 7.6 Metal Foam UTRC Test 14 Data

Mass Flow lbm/s	ReK -	Inlet Temp F	Outlet Temp F	ΔP psi
0.010	21.38	95.08	152.50	0.103
0.010	21.08	86.55	177.92	0.100
0.020	43.61	78.90	167.75	0.230
0.030	67.92	74.63	155.60	0.370
0.040	90.72	72.08	146.49	0.495
0.050	114.14	70.61	139.34	0.622
0.060	136.83	69.36	133.49	0.738
0.070	160.76	68.64	128.87	0.859
0.080	182.90	68.16	125.23	0.972
0.090	206.98	67.65	121.67	1.094
0.099	229.85	67.08	118.92	1.208
0.110	254.53	66.93	116.52	1.330
0.099	229.72	67.31	118.68	1.210
0.089	206.09	67.89	121.76	1.088
0.079	182.71	68.61	125.30	0.965
0.070	159.48	69.64	129.51	0.838
0.060	135.79	70.44	134.35	0.718
0.050	112.67	71.73	140.14	0.595
0.040	89.35	73.61	147.17	0.453
0.029	66.01	76.02	156.24	0.298
0.020	44.35	79.36	168.16	0.195
0.010	21.36	86.07	191.65	0.055

Table 7.7 Metal Foam UTRC Test 24 Data

Mass Flow lbm/s	ReK -	Inlet Temp F	Outlet Temp F	ΔP psi
0.000	0.00	66.78	66.84	0.013
0.001	1.94	66.80	66.87	0.014
0.030	73.26	63.32	63.64	0.222
0.060	145.46	61.86	62.08	0.450
0.003	8.18	63.88	66.27	0.017
0.010	22.98	64.19	166.57	0.067
0.020	45.74	63.63	147.22	0.157
0.030	69.18	63.52	136.31	0.251
0.040	92.31	63.65	128.91	0.348
0.050	116.38	63.98	123.42	0.450
0.060	139.39	64.20	119.45	0.546
0.070	163.30	64.46	116.41	0.647
0.080	186.43	64.75	114.63	0.747
0.090	209.82	64.87	112.31	0.848

R05-5.300.0022

0.100	233.64	65.38	110.60	0.955
0.111	257.57	65.86	109.47	1.057
0.100	231.81	66.19	112.35	0.976
0.090	207.90	66.60	115.00	0.896
0.080	184.50	67.05	118.02	0.809
0.070	160.61	67.54	121.86	0.715
0.060	137.55	68.11	126.38	0.621
0.050	113.84	68.76	132.60	0.515
0.040	90.70	69.62	140.38	0.405
0.030	67.95	70.91	151.56	0.290
0.020	43.95	72.92	169.77	0.157
0.010	21.73	78.05	208.49	0.029

Table 7.8 Metal Foam UTRC Test 25 Data

Mass Flow lbm/s	ReK -	Inlet Temp F	Outlet Temp F	ΔP psi
0.006	14.19	73.65	73.77	0.012
0.030	71.79	74.57	74.48	0.249
0.030	72.22	74.02	74.14	0.252
0.060	143.03	74.06	74.18	0.512
0.002	4.85	74.88	76.75	0.014
0.010	22.17	74.01	160.30	0.074
0.020	45.54	73.87	144.43	0.176
0.030	68.70	74.18	135.43	0.280
0.041	92.66	74.52	129.41	0.390
0.050	114.57	74.92	125.06	0.491
0.060	138.32	75.28	121.39	0.599
0.070	161.09	75.62	118.92	0.701
0.080	184.22	76.01	116.94	0.806
0.090	207.67	76.29	113.86	0.911
0.100	230.60	76.51	112.26	1.015
0.109	251.61	76.74	111.15	1.113
0.100	229.96	76.73	112.72	1.035
0.090	206.59	76.76	115.25	0.946
0.080	183.05	76.98	118.03	0.853
0.070	159.74	77.31	121.23	0.758
0.060	136.56	77.59	124.93	0.658
0.050	113.14	77.97	129.18	0.548
0.040	89.84	78.69	136.51	0.433
0.030	66.56	79.77	146.25	0.309
0.020	44.25	81.28	162.05	0.183
0.010	21.76	84.45	192.74	0.048
0.006	13.50	91.37	170.07	-0.007

Table 7.9 Metal Foam UTRC Test 26A Data

Mass Flow lbm/s	ReK -	Inlet Temp F	Outlet Temp F	ΔP psi
0.008	20.35	79.25	80.72	0.015
0.008	20.29	80.79	82.59	0.015
0.010	23.64	78.92	178.97	0.032
0.020	45.82	77.20	174.92	0.116
0.030	69.88	76.79	160.27	0.202
0.040	94.06	76.65	152.20	0.290
0.050	117.89	76.56	145.94	0.376
0.060	142.13	76.72	141.24	0.462
0.070	166.54	77.02	137.83	0.546
0.080	189.99	77.28	134.73	0.630
0.090	213.73	77.67	132.30	0.712
0.100	237.56	78.17	130.18	0.799
0.110	261.57	78.87	128.37	0.881
0.100	236.34	79.19	131.85	0.812
0.090	212.25	79.46	134.66	0.743
0.080	188.08	79.65	138.21	0.669
0.070	163.89	79.87	142.79	0.591
0.060	139.79	80.21	147.55	0.509
0.050	116.81	80.44	153.07	0.426
0.040	92.27	80.98	160.95	0.329
0.030	69.09	81.62	170.39	0.232
0.020	44.63	82.88	187.49	0.124
0.010	22.43	89.53	225.50	0.010

Table 7.10 Metal Foam UTRC Test 27A Data

Mass Flow lbm/s	ReK -	Inlet Temp F	Outlet Temp F	ΔP psi
0.006	15.04	73.92	77.43	0.018
0.010	24.13	73.51	184.28	0.049
0.020	46.88	72.72	166.15	0.132
0.030	69.35	71.66	153.54	0.223
0.041	97.93	71.58	145.78	0.335
0.050	117.90	71.99	141.74	0.409
0.060	143.27	71.54	136.91	0.502
0.070	166.80	71.03	133.25	0.586
0.081	192.16	71.20	130.16	0.677
0.090	215.50	71.67	128.59	0.764
0.100	239.64	72.36	127.03	0.854
0.110	263.78	73.01	122.98	0.939
0.100	239.32	74.05	124.18	0.873
0.090	214.63	73.54	126.76	0.798

R05-5.300.0022

0.080	190.60	73.78	130.31	0.721
0.070	166.53	74.49	134.63	0.641
0.060	141.39	75.13	139.91	0.553
0.050	117.03	76.46	145.78	0.461
0.040	93.60	76.17	153.26	0.364
0.028	64.57	77.40	165.37	0.233
0.020	45.50	79.75	181.89	0.141
0.009	20.94	87.12	219.90	0.021

Table 7.11 Metal Foam UTRC Test 29 Data

Mass Flow lbm/s	ReK -	Inlet Temp F	Outlet Temp F	ΔP psi
0.060	305.16	72.99	73.20	0.364
0.000	0.00	74.51	79.52	0.017
0.010	47.64	72.24	149.08	0.061
0.020	98.64	71.89	136.01	0.128
0.030	147.44	72.81	131.20	0.195
0.040	196.82	72.25	125.57	0.269
0.051	247.27	73.69	122.82	0.347
0.060	293.46	73.77	120.81	0.417
0.070	344.78	72.80	117.18	0.490
0.080	394.07	73.54	115.95	0.560
0.090	444.75	74.32	112.77	0.634
0.100	493.83	75.48	111.62	0.709
0.043	212.15	61.50	113.35	0.319
0.068	335.97	71.15	119.49	0.490
0.110	542.23	76.44	113.49	0.796
0.100	490.22	75.80	115.89	0.734
0.090	441.72	75.40	117.40	0.673
0.080	391.68	74.88	119.51	0.605
0.041	204.07	64.05	124.31	0.318

Table 7.12 Metal Foam UTRC Test 30A Data

Mass Flow lbm/s	ReK -	Inlet Temp F	Outlet Temp F	ΔP psi
0.006	30.25	72.42	77.99	0.015
0.010	45.91	71.43	163.53	0.045
0.020	96.00	70.47	147.12	0.126
0.030	145.69	69.70	138.34	0.203
0.040	195.48	70.79	132.52	0.284
0.050	243.24	71.38	127.59	0.363
0.060	292.81	71.25	123.46	0.447
0.072	350.93	71.61	120.98	0.535
0.081	394.72	72.50	120.97	0.604

0.090	442.09	72.84	118.52	0.681
0.100	492.26	72.51	114.79	0.763
0.111	546.42	72.89	113.83	0.847
0.100	490.30	73.25	116.45	0.776
0.090	440.82	72.83	117.94	0.709
0.080	390.88	72.53	120.06	0.639
0.070	340.44	72.51	124.05	0.563
0.060	292.48	72.37	126.55	0.489
0.050	242.00	72.66	130.94	0.411
0.040	193.05	72.96	137.87	0.328
0.030	144.69	73.66	146.81	0.238
0.020	96.02	74.96	158.98	0.141
0.020	95.81	75.13	155.35	0.143
0.010	44.80	78.97	186.28	0.045

7.2 Single Tube-Row Metal Foam Experimental Data (HS Marston)

Table 7.13 Brazed 20ppi 10% stainless steel with 0.4pps air flow

Barometer	mb	1006	1006	1006	1006	1006	1006	1006	1006	1006
1.3" Orifice Dp	mb	11.7	11.7	11.7	11.7	11.8	11.8	11.8	11.8	11.9
Orifice static	mb	121.8	121.5	122.3	122.3	123.1	123.1	123	123	123.1
Orifice Temp.	°C	31.15	31.375	34.075	34.2	35.1	35.075	35.575	35.6	36.075
Air Flowrate	lb/s	0.06	0.06	0.06	0.06	0.06	0.06	0.06	0.06	0.06
Oilflow Rdg	pps	355	354	531	531	708	708	879	878.6	1061
Oil Flowrate	litre/s	0.20	0.19	0.29	0.29	0.39	0.39	0.48	0.48	0.58
Temp @ Flowmeter	°C	100.7	100.7	101.1	101.1	101.2	101.2	101.3	101.3	101.4
Specific Gravity		0.9255	0.9255	0.9255	0.9255	0.9255	0.9255	0.9255	0.9255	0.9255
Oil Flowrate	kg/s	0.18	0.18	0.27	0.27	0.36	0.36	0.45	0.45	0.54
	lb/s	0.40	0.40	0.60	0.60	0.79	0.79	0.99	0.98	1.19
	lb/min	23.88	23.81	35.72	35.72	47.62	47.62	59.13	59.10	71.37
Oil Inlet Temp	1 °C	100.7	100.7	101.1	101.1	101.2	101.2	101.3	101.3	101.4
	2 °C	100.7	100.7	101.1	101.1	101.2	101.2	101.3	101.3	101.4
Mean	°C	100.7	100.7	101.1	101.1	101.2	101.2	101.3	101.3	101.4
Oil Outlet Temp	1 °C	99.8	99.8	100.4	100.4	100.7	100.7	100.9	100.9	101.1
	2 °C	99.8	99.8	100.4	100.4	100.7	100.7	100.9	100.9	101.1
Mean	°C	99.8	99.8	100.4	100.4	100.7	100.7	100.9	100.9	101.1
Oil DT	°C	0.9	0.9	0.7	0.7	0.5	0.5	0.4	0.4	0.3
Air Inlet Temp	°C	20.1	20.3	20.6	20.7	20.9	21	21	21	21.1
Air Outlet Temp	1 °C	31.9	32.1	33.8	34	34.9	34.8	35.3	35.3	35.9
	2 °C	30.6	30.8	33.3	33.4	34.3	34.3	34.8	34.8	35.2
	3 °C	31	31.2	34.6	34.7	35.7	35.7	36.2	36.2	36.8
	4 °C	31.1	31.4	34.6	34.7	35.5	35.5	36	36.1	36.4
Mean Air Outlet	°C	31.15	31.375	34.075	34.2	35.1	35.075	35.575	35.6	36.075
Air DT	°C	11.05	11.075	13.475	13.5	14.2	14.075	14.575	14.6	14.975

R05-5.300.0022

E.T.D.	°C	80.6	80.4	80.5	80.4	80.3	80.2	80.3	80.3	80.3
Thermal Ratio	Oil	0.01	0.01	0.01	0.01	0.01	0.01	0.00	0.00	0.00
Thermal Ratio	Air	0.14	0.14	0.17	0.17	0.18	0.18	0.18	0.18	0.19

Table 7.14 Brazed 20ppi 10% stainless steel with 0.6pps air flow

Barometer	mb	1011.0	1011	1011.0	1011.0	1011.0	1011.0	1011.0	1011.0	1011.0	1011.0
1.3" Orifice Dp	mb	5.10	5.10	5.10	5.10	5.10	5.10	5.20	5.20	5.20	5.20
Orifice static	mb	58.40	58.40	58.80	58.80	58.60	58.60	58.90	58.90	58.90	58.90
Orifice Temp.	°C	33.60	33.08	36.03	36.23	37.50	38.20	38.03	38.18	38.95	38.93
Air Flowrate	lb/s	0.04	0.04	0.04	0.04	0.04	0.04	0.04	0.04	0.04	0.04
Oilflow Rdg	pps	353.40	352.90	529.00	529.30	706.70	707.00	878.30	878.60	1063.00	1063.00
Oil Flowrate	litre/s	0.19	0.19	0.29	0.29	0.39	0.39	0.48	0.48	0.58	0.58
Temp @ Flowmeter	°C	99.70	99.70	100.00	100.00	100.20	100.20	100.40	100.40	100.35	100.35
Specific Gravity		0.93	0.93	0.93	0.93	0.93	0.93	0.93	0.93	0.93	0.93
Oil Flowrate	kg/s	0.18	0.18	0.27	0.27	0.36	0.36	0.45	0.45	0.54	0.54
	lb/s	0.40	0.40	0.59	0.59	0.79	0.79	0.98	0.98	1.19	1.19
	lb/min	23.77	23.74	35.58	35.60	47.54	47.56	59.08	59.10	71.50	71.50
Oil Inlet Temp 1	°C	99.70	99.70	100.00	100.00	100.20	100.20	100.40	100.40	100.40	100.40
	2 °C	99.70	99.70	100.00	100.00	100.20	100.20	100.40	100.40	100.30	100.30
Mean	°C	99.70	99.70	100.00	100.00	100.20	100.20	100.40	100.40	100.35	100.35
Oil Outlet Temp 1	°C	99.00	99.00	99.40	99.40	99.80	99.80	100.10	100.10	100.10	100.10
	2 °C	99.00	99.00	99.40	99.40	99.80	99.80	100.10	100.10	100.20	100.20
Mean	°C	99.00	99.00	99.40	99.40	99.80	99.80	100.10	100.10	100.15	100.15
Oil DT	°C	0.70	0.70	0.60	0.60	0.40	0.40	0.30	0.30	0.20	0.20
Air Inlet Temp	°C	20.00	19.50	20.10	20.40	20.90	20.90	21.00	21.00	21.60	21.60
Air Outlet Temp 1	°C	34.10	33.40	35.40	35.60	36.80	39.90	37.40	37.50	38.30	38.30
	2 °C	33.00	32.40	35.00	35.30	36.60	36.60	37.20	37.40	38.10	38.10
	3 °C	33.10	32.80	36.40	36.60	38.00	37.90	38.50	38.60	39.50	39.40
	4 °C	34.20	33.70	37.30	37.40	38.60	38.40	39.00	39.20	39.90	39.90
Mean Air Outlet	°C	33.60	33.08	36.03	36.23	37.50	38.20	38.03	38.18	38.95	38.93
Air DT	°C	13.60	13.58	15.93	15.83	16.60	17.30	17.03	17.18	17.35	17.33
E.T.D.	°C	79.70	80.20	79.90	79.60	79.30	79.30	79.40	79.40	78.75	78.75
Thermal Ratio	Oil	0.01	0.01	0.01	0.01	0.01	0.01	0.00	0.00	0.00	0.00
Thermal Ratio	Air	0.17	0.17	0.20	0.20	0.21	0.22	0.21	0.22	0.22	0.22

Table 7.15 Brazed 20ppi 10% stainless steel with 0.8pps air flow

Barometer	mb	1009	1009	1009	1009	1009	1009	1009	1009	1009	1009
1.3" Orifice Dp	mb	23.7	23.6	23.7	23.7	23.8	23.8	23.8	23.8	23.8	23.8
Orifice static	mb	225	227	226	226.3	227.2	226.5	226.7	225.4	226.3	227.1
Orifice Temp.	°C	28.05	28.05	30.4	30.5	31.55	31.65	32.4	32.45	32.9	32.85
Air Flowrate	lb/s	0.08	0.08	0.08	0.08	0.08	0.08	0.08	0.08	0.08	0.08
Oilflow Rdg	pps	353.3	354	531.2	531.2	707.2	707.2	878	878	1063	1063
Oil Flowrate	litre/s	0.19	0.19	0.29	0.29	0.39	0.39	0.48	0.48	0.58	0.58
Temp @ Flowmeter	°C	100.3	100.3	100	99.95	100.5	100.5	100.35	100.3	100.3	100.35
Specific Gravity		0.93	0.93	0.93	0.93	0.93	0.93	0.93	0.93	0.93	0.93
Oil Flowrate	kg/s	0.18	0.18	0.27	0.27	0.36	0.36	0.45	0.45	0.54	0.54
	lb/s	0.40	0.40	0.60	0.60	0.79	0.79	0.98	0.98	1.19	1.19
	lb/min	23.76	23.81	35.73	35.73	47.57	47.57	59.06	59.06	71.50	71.50
Oil Inlet Temp 1	°C	100.3	100.3	100	100	100.5	100.5	100.4	100.3	100.3	100.4
	2 °C	100.3	100.3	100	99.9	100.5	100.5	100.3	100.3	100.3	100.3
Mean	°C	100.3	100.3	100	99.95	100.5	100.5	100.35	100.3	100.3	100.35
Oil Outlet Temp 1	°C	99.3	99.3	99.2	99.1	99.9	99.8	99.8	99.8	100	100
	2 °C	99.3	99.3	99.2	99.2	99.8	99.8	99.8	99.8	100	100
Mean	°C	99.3	99.3	99.2	99.15	99.85	99.8	99.8	99.8	100	100
Oil DT	°C	1	1	0.8	0.8	0.65	0.7	0.55	0.5	0.3	0.35
Air Inlet Temp	°C	18.9	18.8	18.8	18.9	18.9	19	19.3	19.4	19.5	19.5
Air Outlet Temp 1	°C	28.6	28.6	30	30.1	31.1	31.2	32	32	32.5	32.4
	2 °C	27.5	27.5	29.5	29.6	30.8	30.9	31.6	31.7	32.1	32.1
	3 °C	27.5	27.6	30.6	30.7	31.9	32	32.9	32.9	33.4	33.4
	4 °C	28.6	28.5	31.5	31.6	32.4	32.5	33.1	33.2	33.6	33.5
Mean Air Outlet	°C	28.05	28.05	30.4	30.5	31.55	31.65	32.4	32.45	32.9	32.85
Air DT	°C	9.15	9.25	11.6	11.6	12.65	12.65	13.1	13.05	13.4	13.35
E.T.D.	°C	81.4	81.5	81.2	81.05	81.6	81.5	81.05	80.9	80.8	80.85
Thermal Ratio	Oil	0.01	0.01	0.01	0.01	0.01	0.01	0.01	0.01	0.00	0.00
Thermal Ratio	Air	0.11	0.11	0.14	0.14	0.16	0.16	0.16	0.16	0.17	0.17

Table 7.16 Brazed 20ppi 10% stainless steel with 1.0 pps air flow

Barometer	mb	1000	1000	1000	1000	1000	1000	1000	1000	1000	1000
1.3" Orifice Dp	mb	49.5	49.7	49.6	49.7	49.8	49.9	49.4	49.7	50.1	50.3
Orifice static	mb	401.4	402.1	402.1	404.2	4403.6	404.3	399.7	402.5	401.6	403.3
Orifice Temp.	°C	26.025	25.8	28.725	28.725	29.925	29.975	30.95	30.875	31.45	31.5
Air Flowrate	lb/s	0.10	0.10	0.10	0.10	0.10	0.10	0.01	0.10	0.10	0.10
Oilflow Rdg	pps	352.8	354.7	531.7	533.1	705.4	706.1	878.8	879.3	1062	1063
Oil Flowrate	litre/s	0.19	0.19	0.29	0.29	0.39	0.39	0.48	0.48	0.58	0.58
Temp @ Flowmeter	°C	99.7	99.7	100.1	100.1	100.1	100.1	100.3	100.25	100.1	100.1
Specific Gravity		0.93	0.93	0.93	0.93	0.93	0.93	0.93	0.93	0.93	0.93
Oil Flowrate	kg/s	0.18	0.18	0.27	0.27	0.36	0.36	0.45	0.45	0.54	0.54
	lb/s	0.40	0.40	0.60	0.60	0.79	0.79	0.99	0.99	1.19	1.19

	lb/min	23.73	23.86	35.77	35.86	47.45	47.50	59.11	59.15	71.44	71.50
Oil Inlet Temp 1	°C	99.7	99.7	100.1	100.1	100.1	100.1	100.3	100.3	100.1	100.1
	2 °C	99.7	99.7	100.1	100.1	100.1	100.1	100.3	100.2	100.1	100.1
Mean	°C	99.7	99.7	100.1	100.1	100.1	100.1	100.3	100.25	100.1	100.1
Oil Outlet Temp 1	°C	98.6	98.7	99.3	99.2	99.4	99.4	99.7	99.7	99.7	99.6
	2 °C	98.6	98.7	99.3	99.2	99.4	99.4	99.7	99.7	99.7	99.7
Mean	°C	98.6	98.7	99.3	99.2	99.4	99.4	99.7	99.7	99.7	99.65
Oil DT	°C	1.1	1	0.8	0.9	0.7	0.7	0.6	0.55	0.4	0.45
Air Inlet Temp	°C	18	18	18.4	18.3	18.5	18.6	19	19.1	19.3	19.4
Air Outlet Temp 1	°C	26.7	25.6	28.4	28.4	29.6	29.6	30.7	30.6	31.1	31.2
	2 °C	25.5	25.5	27.9	27.9	29.3	29.4	30.3	30.3	30.7	30.8
	3 °C	25.4	25.5	28.8	28.8	30.1	30.1	31.1	31	31.8	31.7
	4 °C	26.5	26.6	29.8	29.8	30.7	30.8	31.7	31.6	32.2	32.3
Mean Air Outlet	°C	26.03	25.80	28.73	28.73	29.93	29.98	30.95	30.88	31.45	31.50
Air DT	°C	8.03	7.80	10.33	10.43	11.43	11.38	11.95	11.78	12.15	12.10
E.T.D.	°C	81.7	81.7	81.7	81.8	81.6	81.5	81.3	81.15	80.8	80.7
Thermal Ratio	Oil	0.01	0.01	0.01	0.01	0.01	0.01	0.01	0.01	0.00	0.01
Thermal Ratio	Air	0.10	0.10	0.13	0.13	0.14	0.14	0.15	0.15	0.15	0.15

Table 7.17 Brazed 20ppi 10% stainless steel pressure drop

Reading No.		1	2	3	4	5	6	7	8	9
Barometer	mb	978	978	978	996	996	996	996	996	996
Orifice Dp	mb	164.00	126.00	84.00	56.00	37.3	24.8	16.5	11.1	7.4
Orifice static	mb	663.0	626.0	542.0	425.0	320.0	230.0	163.0	114.0	79.0
Orifice Temp.	°C	17.2	17.2	17.2	19.7	19.9	20.0	20.2	20.1	21.3
	K	290.2	290.2	290.2	292.7	292.9	293.0	293.2	293.1	294.3
Air Flowrate	lb/s	0.115	0.113	0.109	0.105	0.0941	0.0823	0.0703	0.0596	0.0496
Airside Dp	mb	660.0	624.0	540.0	428.0	321.5	231.5	164.0	115.0	79.0

Table 7.18 No-Braze 20ppi 10% stainless steel pressure drop

Reading No.		1	2	3	4	5	6	7	8	9
Barometer	mb	973	973	973	973	973	973	973	973	973
Orifice Dp	mb	160.40	126.00	84.00	56.00	37.3	24.8	16.5	11.1	7.4
Orifice static	mb	596.1	550.3	456.3	348.2	255.5	182.3	126.6	89.6	61.9
Orifice Temp.	°C	21.4	20.9	21.0	21.1	21.1	20.9	21.0	20.9	20.9

R05-5.300.0022

11 29.5 290 1.31 297

Open Cellular Unit, D6727-250B

No.	Orifice Delta P (mb)	Inlet Pressure (mb)	Flow (lb/s)	Raw Unit Delta P (mb)
1	1.25	12.1	0.32	12.2
2	2.28	22.3	0.43	22.5
3	3.54	32.0	0.53	32.7
4	4.69	44.0	0.61	44.5
5	6.1	60	0.69	62
6	9.0	89	0.82	91
7	12.0	120	0.93	123
8	15.4	152	1.04	155
9	20.0	192	1.15	197

Table 7.21 Plain aligned and staggered tube bank pressure drop data

Barometer Reading 1001 mb Air Temp = 20°C

Plain In-Line Unit, D6727-100B

No.	Orifice Delta P (mb)	Inlet Pressure (mb)	Flow (lb/s)	Raw Unit Delta P (mb)
1	1.39	7.9	0.33	8.0
2	2.95	31.5	0.48	32.5
3	5.0	55.0	0.62	57
4	7.0	74	0.73	76
5	11.3	130	0.89	133
6	16.8	182	1.05	186
7	24.1	258	1.20	264

Plain Staggered Unit, D6727-150B

No.	Orifice Delta P (mb)	Inlet Pressure (mb)	Flow (lb/s)	Raw Unit Delta P (mb)
1	1.18	13.0	0.31	13.2
2	2.87	29.0	0.48	29.6
3	5.00	53.0	0.62	55.0
4	7.2	71	0.74	74
5	11.4	111	0.91	114
6	16.5	155	1.06	160
7	24.0	216	1.23	223
8	28.6	252	1.31	254

R05-5.300.0022

Table 7.22 Aligned and staggered metal foam pressure drop data

Barometer Reading	992 mb	Air Temp =	18°C	
In Line Metal Foam Unit, D6727-300B				
No.	Orifice Delta P (mb)	Inlet Pressure (mb)	Flow (lb/s)	Raw Unit Delta P (mb)
1	0.40	16	0.18	16
2	1.39	55	0.33	54
3	4.02	144	0.53	145
4	8.0	270	0.69	272
5	13.0	393	0.80	397
6	16.9	473	0.84	477

Barometer Reading	1007 mb	Air Temp =	18°C	
Staggered Metal Foam Unit, D6727-350B				
No.	Orifice Delta P (mb)	Inlet Pressure (mb)	Flow (lb/s)	Raw Unit Delta P (mb)
1	0.43	17	0.18	16.0
2	1.03	39	0.28	39.5
3	3.05	112	0.47	113
4	6.0	210	0.63	212
5	10.0	325	0.75	327
6	17.3	483	0.85	487

7.3.2 Heat Transfer Performance

Table 7.23 Dense cellular metal heat transfer performance data

No:	1	2	3	4	5
Orifice DeltaP (mb)	120	67	33.3	16.1	5.3
Inlet DeltaP (mb)	268	149	75	37	12.7
Flow (lb/s)	1.176	0.847	0.583	0.401	0.230
Air Temp In 1 (C)	30.7	31.4	32.4	32.4	32.4
Air Temp In 2 (C)	30.3	31.2	32.4	32.3	32.3
Av. Air Temp In (C)	30.5	31.3	32.4	32.4	32.4
Air Temp Out 1(C)	45.8	49.9	54.2	57.7	63.1
Air Temp Out 2 (C)	46.3	50.2	54.8	58.4	63.7
Air Temp Out 3 (C)	46.6	50.5	54.8	58.4	63.8
Av. Air Temp Out (C)	46.2	50.2	54.6	58.2	63.5
Waterflow (ppl)	919	887	860	851	845
Waterflow (lb/s)	0.636	0.614	0.595	0.589	0.585

R05-5.300.0022

W Temp In 1 (C)	88.5	88.8	89.1	88.7	89.0
W Temp In 2 (C)	89.1	89.5	89.7	89.3	89.7
Av. W Temp In (C)	88.8	89.2	89.4	89.0	89.4
W Temp Out 1 (C)	81.5	82.9	84.2	84.8	86.3
W Temp Out 2 (C)	81.8	83.1	84.5	85.0	86.6
Av. W Temp Out (C)	81.7	83.0	84.4	84.9	86.5

Table 7.24 Open cellular metal heat transfer performance data

No:	1	2	3	4	5
Orifice DeltaP (mb)	110	60	30.7	15.1	5.2
Inlet DeltaP (mb)	237	123	57	30	10
Flow (lb/s)	1.121	0.799	0.560	0.390	0.228
Air Temp In 1 (C)	26.1	26.3	26.9	27.3	27.7
Air Temp In 2 (C)	25.9	26.3	27	27.6	27.8
Av. Air Temp In (C)	26.0	26.3	27.0	27.5	27.8
Air Temp Out 1(C)	43.1	45.6	48	52.5	55.9
Air Temp Out 2 (C)	42.9	45.2	47.8	52.2	55.5
Air Temp Out 3 (C)	42	44.8	47.6	51.8	55.2
Av. Air Temp Out (C)	42.7	45.2	47.8	52.2	55.5
Waterflow (ppi)	1054	1032	1009	1006	990
Waterflow (lb/s)	0.729	0.714	0.698	0.696	0.685
W Temp In 1 (C)	89.2	89.3	89.7	89.8	89.8
W Temp In 2 (C)	90	90	90.1	90.3	90.3
Av. W Temp In (C)	89.6	89.7	89.9	90.1	90.1
W Temp Out 1 (C)	83.5	84.6	85.9	86.7	87.8
W Temp Out 2 (C)	83.2	84.3	85.5	86.4	87.5
Av. W Temp Out (C)	83.4	84.5	85.7	86.6	87.7

Table 7.25 Aligned metal foam heat transfer performance data

Baro =	1002	mb			
No:	1	2	3	4	5
Or Delta P (mb)	111	67.0	31.5	15.7	5.0
Or St (mb)	722	413	184	91	30.3
Flow (lb/s)	1.367	0.969	0.614	0.419	0.232
Air Temp In 1 (C)	19.9	22.8	24.4	24.8	25.4
Air Temp In 2 (C)	20	22.8	24.4	24.9	25.4
Av. Air Temp In (C)	20.0	22.8	24.4	24.9	25.4
Air Temp Out 1(C)	38.6	43.1	46.6	49.7	55.5
Air Temp Out 2 (C)	39.9	44.8	48.5	51.8	58.1
Air Temp Out 3 (C)	40.1	44.9	48.5	51.8	58.1
Av. Air Temp Out (C)	39.5	44.3	47.9	51.1	57.2

R05-5.300.0022

Waterflow (ppl)	2321	2322	2317	2321	2316
Waterflow (lb/s)	2.713	2.714	2.708	2.713	2.707
Av. W Temp In (C)	90.6	91.0	88.9	89.0	90.3
Av. W Temp Out (C)	88.2	89.1	87.5	87.9	89.5

Table 7.26 Staggered metal foam heat transfer performance data

Baro =	1003		mb		
No:	1	2	3	4	5
Or Delta P (mb)	110	65.7	32.0	15.8	5.1
Or St (mb)	721	403	188	92	31.5
Flow (lb/s)	1.347	0.947	0.614	0.416	0.232
Air Temp In 1 (C)	25.6	26.1	26.1	26.9	27.0
Air Temp In 2 (C)	25.6	26.1	26.2	27.0	27.1
Av. Air Temp In (C)	25.6	26.1	26.2	27.0	27.1
Air Temp Out 1(C)	46.2	48.7	52.1	55.8	61.5
Air Temp Out 2 (C)	48.2	51.3	55.5	59.8	66.3
Air Temp Out 3 (C)	52.0	55.3	59.9	64.9	70.4
Av. Air Temp Out (C)	48.8	51.8	55.8	60.2	66.1
Waterflow (ppl)	2323	2336	2328	2325	2328
Waterflow (lb/s)	2.715	2.731	2.721	2.718	2.721
Av. W Temp In (C)	89.8	88.9	89.2	89.5	89.1
Av. W Temp Out (C)	87.3	86.8	87.7	88.3	88.3

Table 7.27 Plain aligned tube-bank heat transfer performance data

Baro =	999		mb		
No:	1	2	3	4	5
Or Delta P (mb)	109	63.3	30.7	15.2	4.9
Or St (mb)	244	135	66.8	30.2	6.8
Flow (lb/s)	1.142	0.834	0.569	0.396	0.224
Air Temp In 1 (C)	22.7	25.3	25.8	25.8	25.7
Air Temp In 2 (C)	22.7	25.4	25.9	25.8	25.7
Av. Air Temp In (C)	22.7	25.4	25.9	25.8	25.7
Air Temp Out 1(C)	37.3	42.2	45.2	47.0	52.3
Air Temp Out 2 (C)	39.3	44.8	49.3	50.6	52.2
Av. Air Temp Out (C)	38.3	43.5	47.3	48.8	52.3
Av. Air Temp Out (C)	38.3	43.5	47.3	48.8	52.3
Ave T (K)	303.7	307.6	309.7	310.5	312.1
Cp	1006.3	1006.5	1006.6	1006.6	1006.7
Eff	23%	28%	33%	36%	40%

R05-5.300.0022

Waterflow (ppl)	831	831	831	831	831
Waterflow (lb/s)	2.473	2.473	2.473	2.473	2.473
Av. W Temp In (C)	89.6	91.3	91.5	89.8	91.6
Av. W Temp Out (C)	87.1	89.3	89.7	88.3	90.5

Table 7.28 Plain staggered tube-bank heat transfer performance data

Baro =	1014		mb		
No:	1	2	3	4	5
Or Delta P (mb)	116	62.0	30.3	14.3	5.1
Or St (mb)	234	123.8	60.0	28.0	10.7
Flow (lb/s)	1.175	0.830	0.569	0.387	0.231
Air Temp In 1 (C)	22	23.5	24.5	25.5	25.7
Air Temp In 2 (C)	22	23.6	24.5	25.5	25.7
Av. Air Temp In (C)	22.0	23.6	24.5	25.5	25.7
Air Temp Out 1(C)	42.4	45.3	48.9	52.9	58.6
Air Temp Out 2 (C)	42.5	44.5	48.8	52.8	58.5
Air Temp Out 3 (C)	42.4	45.2	48.4	52.7	58.5
Av. Air Temp Out (C)	42.4	45.0	48.7	52.8	58.5
Ave T (K)	305.4	307.4	309.8	312.3	315.3
Cp	1006.4	1006.5	1006.6	1006.7	1006.9
Eff	29%	31%	36%	42%	50%
Waterflow (ppl)	830	830	830	830	830
Waterflow (lb/s)	2.470	2.470	2.470	2.470	2.470
Av. W Temp In (C)	92.8	92.1	92.3	90.9	91.5
Av. W Temp Out (C)	90.1	89.8	90.4	89.3	90.2

7.4 CFD Results

Table 7.29 Dense cellular metal CFD prediction for a single periodic element

Mass Flow kg/s	dP/dx (kPa/m)	Heat Flux (W)
0.0005	422	2.157
0.0004	276	1.884
0.0003	162	1.588
0.0002	77	1.253

Table 7.30 Dense aligned cellular metal CFD prediction for a single periodic element

Mass Flow kg/s	dP/dx (kPa/m)	Heat Flux (W)
0.0005	549	1.18

Table 7.31 Open cellular metal CFD prediction for a single periodic element

Mass Flow kg/s	dP/dx (kPa/m)	Heat Flux (W)
0.00105	495	4.181
0.0009	367	3.804
0.00075	259	3.407

Table 7.32 Open elliptical cellular metal CFD prediction for a single periodic element

Mass Flow kg/s	dP/dx (kPa/m)	Heat Flux (W)
0.00105	377	4.04
0.0009	279	3.676
0.00075	195	3.281

Table 7.33 Open staggered cellular metal CFD prediction for a single periodic element

Mass Flow kg/s	dP/dx (kPa/m)	Heat Flux (W)
0.00105	506	4.342
0.0009	375	3.938
0.00075	264	3.516

Table 7.34 Aligned tube-bank reference CFD prediction for a single periodic element

Mass Flow kg/s	dP/dx (kPa/m)	Heat Flux (W)
0.0005	234	1.567
0.0004	144	1.336
0.0003	70	1.037
0.0002	28	0.7609

7.5 Full-Size Demonstration Unit

After the completion of the single tube-row experiments, an engine demonstration unit was designed with the available information to investigate the metal foam heat transfer and pressure drop behavior more accurately. The design was completed, but not fabricated as the engine demonstration schedule changed and the metal foam performance benefit compared to the conventional shell tube was projected to be minimal. The tube-bank testing was performed in place of an engine demonstration. A complete manufacturing drawing package was completed with the general arrangement show in Figures 7.1 and 7.2.

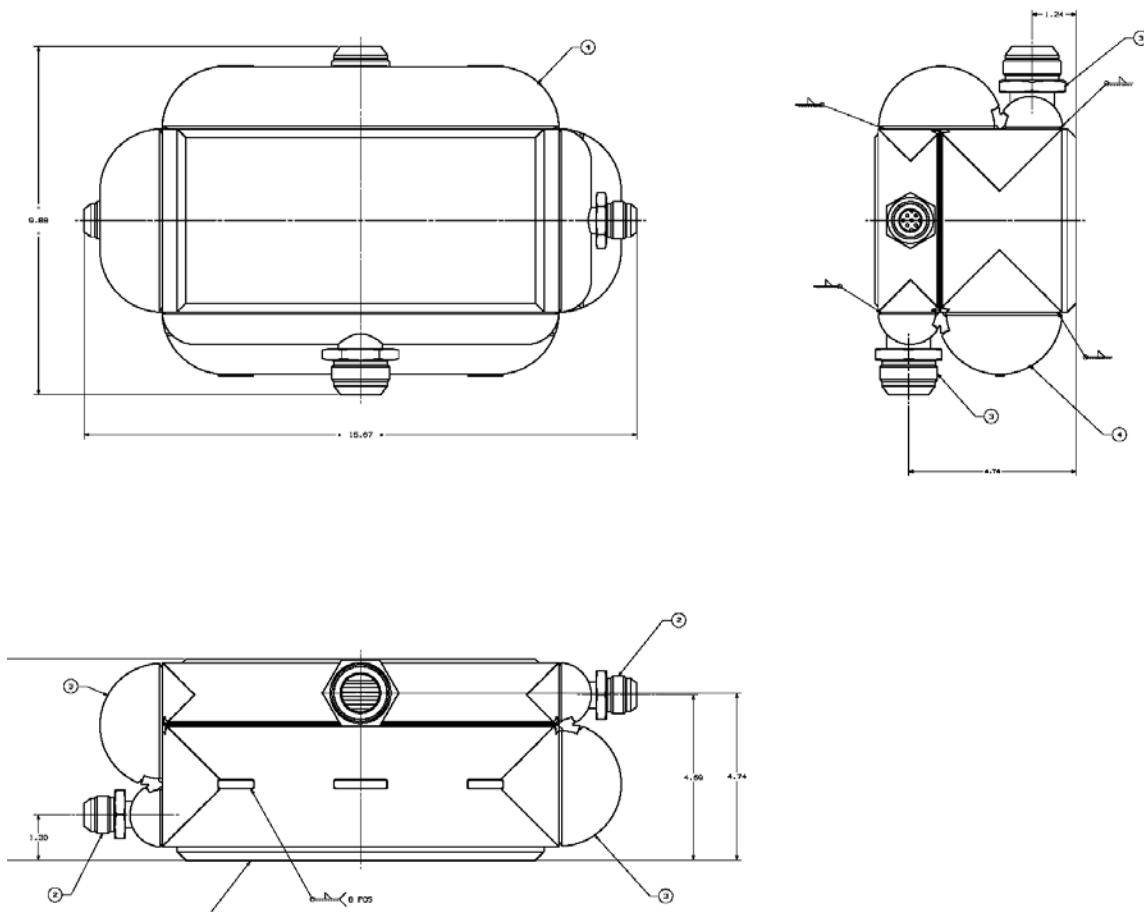


Figure 7.1 General arrangement of metal foam engine demonstration unit

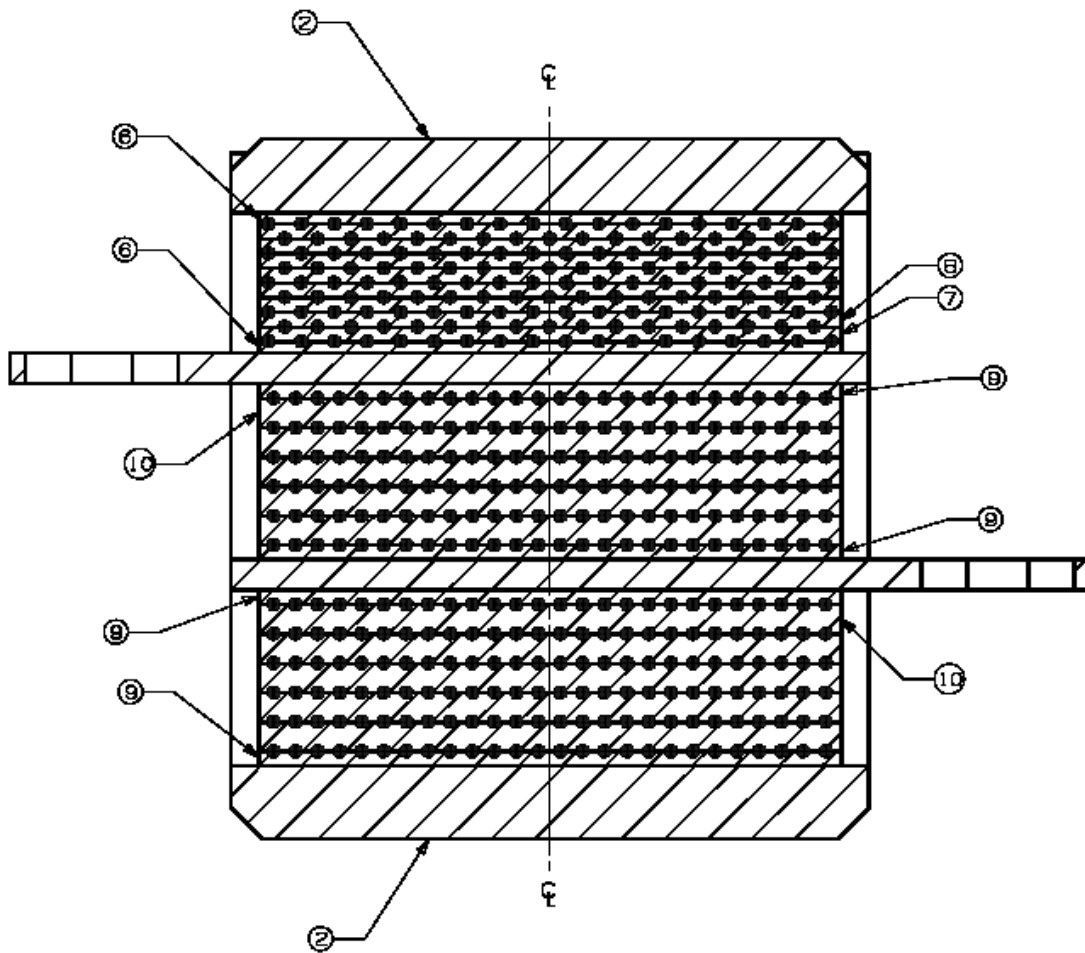


Figure 7.2 Cross section of metal foam engine demonstration unit showing 3 air passes with both aligned and staggered tube arrangements